

Fatigue Monitoring System of a Tension Leg Platform for Floating Offshore Wind Turbines

Master of Science Thesis

Marina Cerdà Alonso



Fatigue Monitoring System of a Tension Leg Platform for Floating Offshore Wind Turbines

by

Marina Cerdà Alonso

Performed at

Bluewater Energy Services

to obtain the degree of Master of Science in Marine Technology at the Delft University of Technology.

to be defended publicly on Friday August 18, 2023 at 10:15 AM.

Thesis number: MT.22/23.043.M

Company supervisor

Responsible supervisor: Dr. ir. J.J. van der Cammen

E-mail: Jeroen.vanderCammen@bluewater.com

Thesis Exam Committee

Chair/Responsible Professor: Dr. ir. L. Pahlavan

Committee Member: Dr. C. L. Walters

Committee Member: Dr. A. Grammatikopoulos

Committee Member: MSc. F. Riccioli

Committee Member: Dr. ir. J.J. van der Cammen

Author Details

Student Number: 5626005

Author contact e-mail: marinacerdaa@gmail.com

Preface

This thesis was conducted to obtain the master's degree in Marine Technology with the specialization of Ship and Offshore Structures at the Delft University of Technology. It was performed in collaboration of Bluewater Energy Services.

First, I would like to thank Pooria Pahlavan for his invaluable guidance throughout the project. His positive attitude made the process smoother. Moreover, I appreciate the opportunity he provided, allowing me to delve into the world of maritime structures.

I would also like to extend my thanks Jeroen van der Cammen for his continuous mentorship, from which I did not only learn technical skills. My gratitude goes as well for the Naval and Structural sections of Bluewater, for presenting me with the chance to conduct research on such a interesting topic.

Likewise, I would like to thank Filippo Riccioli, who generously invested his time to assist me. His advice were very helpful to refining my work. Furthermore, I would like to thank Apostolos Grammatikopoulos for the feedback he provided in the final months.

Finally, I would like to thank my family, friends and boyfriend. Their unconditional support were key in my journey. Reaching this point would have been significantly more challenging without their persistent motivation and love.

M. Cerdà Alonso
Delft, August 2023

Abstract

Floating Offshore Wind Turbines (FOWTs) have emerged as a promising technology for generating clean energy in deep water locations. Bluewater Energy Services proposes a Tension Leg Platform (TLP) as the floating support structure. An effective Structural Health Monitoring (SHM) system (of which there are various types) can facilitate timely interventions and optimize inspection and maintenance activities by providing continuous insights into their structural condition. Fatigue damage is especially critical for the support structures of FOWTs, as they are subject to cyclic loads that can cause structural damage.

This research proposes a fatigue monitoring system for a TLP supporting FOWTs. The methodology used is Modal Decomposition and Expansion (MDE). Due to the complexity of the studied structure in terms of structural dynamics, MDE is selected for its ability to capture dynamic behaviour. The main objective of the fatigue monitoring system is to perform the full-field strain estimation based on a limited number of sensors. This could also allow for the verification of the design considerations. With the presented response reconstruction approach, the stress in the locations prone to fatigue of the platform can be monitored and therefore, enabling estimation of the remaining lifetime of the structure and optimize maintenance planning.

Different analytical and numerical models are used in this investigation. The application of MDE in a simple structure (i.e. a cantilever beam) is first assessed to verify the performance and to gain insights of the methodology. Later, MDE is applied to a simplified TLP model to validate the response reconstruction approach and demonstrate its applicability for TLP-like structures.

Finally, a FOWT numerical model is used to design the fatigue monitoring system. The proposed system consists of two layouts of two strain gauges in the upper column of the TLP, and two layouts of two strain gauges on each pontoon. This system can provide full-field strain estimations with over 88.9% accuracy and predict fatigue damage accumulation with errors of less than 0.01%. Also, the system presented in this thesis only predicts global responses. However, the fatigue of the structure is also influenced by local structural responses due to sea pressures. Therefore, future research to include local effects in the predictions is recommended.

Nomenclature

Abbreviations

AMS	Asset Management System
BES	Bluewater Energy Services
COV	Coefficient of Variation
DNV	Det Norske Veritas
DOF	Degree of Freedom
FE	Finite Element
FOWT	Floating Offshore Wind Turbine
FPSO	Floating Production Storage and Offloading
JIP	Joint Industry Project
LCoE	Levelized Cost of Energy
MDE	Modal Decomposition and Expansion
MSE	Mean Squared Error
O&G	Oil and Gas
O&M	Operation and Maintenance
OMA	Operational Modal Analysis
OWT	Offshore Wind Turbine
SCADA	Supervisory Environmental Control and Data Acquisition
SHM	Structural Health Monitoring
TLP	Tension Leg Platform
VIM	Vortex-Induced Motion
VIV	Vortex-Induced Vibration

Mathematical Symbols

$\vec{\mathbf{n}}_{z,e}$	Z-component of the element normal vector
$[\bullet]^\dagger$	Moore-Penrose pseudo-inverse

\bar{a}	Intercept of the design S-N curve with the log N axis
$\ddot{\mathbf{u}}(t)$	Acceleration vector
$\dot{\mathbf{u}}(t)$	Velocity vector
$\hat{\boldsymbol{\epsilon}}$	Estimated full-field strain
$\hat{\boldsymbol{\epsilon}}_m$	Strain measurements
$\hat{\boldsymbol{\Phi}}$	Truncated and estimated modal matrix
$\hat{\boldsymbol{\Phi}}_m(t)$	Estimated modal matrix for measured DOFs
$\hat{\boldsymbol{\Phi}}_p(t)$	Estimated modal matrix for predicted DOFs
$\hat{\boldsymbol{\Phi}}_{\epsilon,m}(t)$	Estimated strain modal matrix for measured DOFs
$\hat{\boldsymbol{\Phi}}_{\epsilon,p}(t)$	Estimated strain modal matrix for predicted DOFs
$\hat{\boldsymbol{\Phi}}_{\epsilon}(t)$	Estimated strain modal matrix
$\hat{\mathbf{q}}$	Estimated modal coordinates
$\hat{\mathbf{u}}(t)$	Estimated displacement vector
$\hat{\mathbf{u}}_m(t)$	Estimated displacement vector for measured DOFs
$\hat{\mathbf{u}}_p(t)$	Estimated displacement vector for predicted DOFs
$\boldsymbol{\phi}$	Mode shape vector
$\boldsymbol{\Phi}_m$	Modal matrix for measured DOFs
$\boldsymbol{\Phi}_p$	Modal matrix for predicted DOFs
\mathbf{a}_b	Body acceleration relative to earth
\mathbf{a}_f	Fluid acceleration relative to earth
\mathbf{C}	Damping matrix
$\mathbf{f}(t)$	External force vector
\mathbf{K}	Stiffness matrix
\mathbf{M}	Mass matrix
$\mathbf{u}(t)$	Displacement vector
$\mathbf{u}_m(t)$	Displacement vector for measured DOFs
$\mathbf{u}_p(t)$	Displacement vector for predicted DOFs
\mathbf{v}_f	Fluid velocity relative to earth
\mathbf{v}_r	Fluid velocity relative to the body

$\Delta\sigma_i$	Stress range block
Δ	Mass of the fluid displaced by the body
δ	Change in length
γ	Peak enhancement factor
κ	Curvature
ω	Natural frequency
ρ	Density
σ_x	Axial stress
σ_y	Bending stress
σ_{xy}	Shear stress
θ	Rotation
ε	Strain
ε_{axial}	Strain due to axial response
$\varepsilon_{bending}$	Strain due to bending response
$\varepsilon_{estimated}$	Estimated strain
$\varepsilon_{numerical}$	Numerical strain
ε_{zz}	Strain in z direction
A	Drag area
A	Surface area
A, B	Constants to define the modal coordinate
$ampl$	Scaled mean value of the amplitudes of the mode shapes
B	Buoyancy
C_a	Added mass coefficient for the body
C_d	Drag coefficient for the body
C_d^*	OrcaFlex drag coefficient
C_m	Inertia coefficient for the body
C_{ampl}	Coefficient of contribution of $ampl$ in minimizing the error
C_{diff}	Coefficient of contribution of $diff$ in minimizing the error
C_{dir}	Current direction

C_{sim}	Coefficient of contribution of sim in minimizing the error
D	Accumulated fatigue damage
D	Diameter
D_{error}	Error in the fatigue damage accumulation
$diff$	Scaled mean distance between the mode shapes
E	Young's Modulus
e	Element
EA	Axial stiffness
EI	Bending stiffness
f	Fluid force (per unit length) on the body
g	Gravity
h_e	Depth of the point
H_s	Significant wave height
I_x, I_y, I_z	Mass moment of inertia
k	Number of stress blocks
L	Original length
l	Length
M	Moment
M	Number of modes considered
m	Negative inverse slope of the S-N curves
m_e	shell element mass
m_{added}	Added mass
N	Number of DOFs
N	Number of cycles
N_i	Number of cycles to failure at constant stress range $\Delta\sigma_i$
n_i	Number of stress blocks
N_m	Number of measured DOFs
N_p	Number of predicted DOFs
Occ	Probability of occurrence

p_e	Hydrostatic pressure per element
q	Modal coordinate
$S(\Phi)$	Vector space (where the response of a structure is situated)
s_σ	Estimation error in the standard deviation
sim	Scaled distance between the response and the closest mode shape
t	Thickness
t	Time stamp
T_p	Wave period
V	Volume
V_c	Current speed
V_w	Wind speed
Wav_{dir}	Wave direction
Win_{dir}	Wind direction
y	Distance from the neutral axis
$S(\Phi)$	Linear subspace (where the estimated response is situated)

Contents

Preface	ii
Abstract	iv
1 Introduction	1
1.1 Background and Motivation	1
1.1.1 Tension Leg Platforms for Offshore Wind Energy	1
1.1.2 Structural Health Monitoring for Fatigue in Offshore Structures	2
1.2 Preliminary Knowledge	3
1.2.1 Tension Leg Platform	3
1.2.2 Loads	5
1.3 Literature Review	6
1.3.1 Force Identification	7
1.3.2 Response Estimation or Virtual Sensing	7
1.3.3 Literature Review Conclusions	11
1.4 Knowledge Gap and Research Direction	11
1.4.1 Knowledge Gap	11
1.4.2 Research Direction	11
1.5 Report Outline and Collaboration Partner	12
1.5.1 Report Outline	12
1.5.2 Collaboration Partner	12
2 Methodology	13
2.1 Mathematical framework	13
2.1.1 Modal Decomposition	13
2.1.2 Modal Expansion	15
2.2 Approach	15
3 Analysis and Results	17
3.1 Simplified TLP	17
3.1.1 Introduction and Objective	17
3.1.2 Model	17
3.1.3 Results	18
3.1.4 Conclusions	21
3.2 FOWT	21
3.2.1 Introduction and Objective	21
3.2.2 Model	22
3.2.3 Results	26

3.2.4	Conclusions	37
4	Design of Fatigue Monitoring System	38
4.1	Modal Selection	38
4.1.1	Strain Energy	38
4.1.2	Similarity	39
4.2	Sensor Layout Selection	39
4.2.1	Sensor Placement General Guidance.	39
4.2.2	Optimization Algorithm for Longitudinal Placement	40
4.3	Updated Design.	41
4.3.1	Upper Column	41
4.3.2	Pontoons	42
4.3.3	Measuring Rate (or Sampling Rate)	43
4.3.4	Model Validation	43
4.3.5	Limitations	44
4.3.6	Accuracy	44
5	Sensitivity Analysis	46
5.1	Number of Modes and Sensors	46
5.1.1	Number of Sensors	46
5.1.2	Number of Modes.	47
5.1.3	Conclusions	48
5.2	Unknown Loading Conditions	48
5.2.1	Modal Selection.	48
5.2.2	Sensor Placement	49
5.2.3	Conclusions	49
5.3	Mass Distribution.	49
5.3.1	Point Masses	49
5.3.2	Added Mass.	49
5.3.3	Conclusions	50
5.4	Measurement Error	50
5.4.1	Conclusions	51
6	Conclusions and Future Recommendations	52
6.1	Conclusions	52
6.2	Future Recommendations	53
	Bibliography	55
A	Critical Locations BES TLP Model	60
B	Application of MDE to Simple Structure	62
B.1	Analytical Model	62
B.1.1	Introduction and Objective	62
B.1.2	Model	62
B.1.3	Results	63

B.2	FE Model	65
B.2.1	Introduction and Objective	65
B.2.2	Model	65
B.2.3	Results	66
B.2.4	Sensitivity Analysis	67
B.2.5	Number of Sensors	67
B.2.6	Conclusions	71
C	Response Analysis	72

Introduction

1.1. Background and Motivation

1.1.1. Tension Leg Platforms for Offshore Wind Energy

Offshore wind energy offers a feasible solution for the production of renewable energy. Offshore Wind Turbines (OWTs) provide advantages in comparison with onshore wind turbines, such as high and consistent wind speeds, reduced noise, vibration, and visual impact, and increased capacity [1]. OWTs can have different kinds of support structures, typically classified as bottom-fixed and floating. The former solution is widely preferred for shallow waters. While the latter is employed in deeper waters (>50m) such as Floating Offshore Wind Turbines (FOWTs). This is of relevance since more than 75% of the world's offshore wind potential is located in areas where the water depth is larger than 60 meters [2]. There are several types of floating support structures, including semi-submersible platforms, spars, barges, and Tension Leg Platforms (TLPs). Figure 1.1 illustrates them.

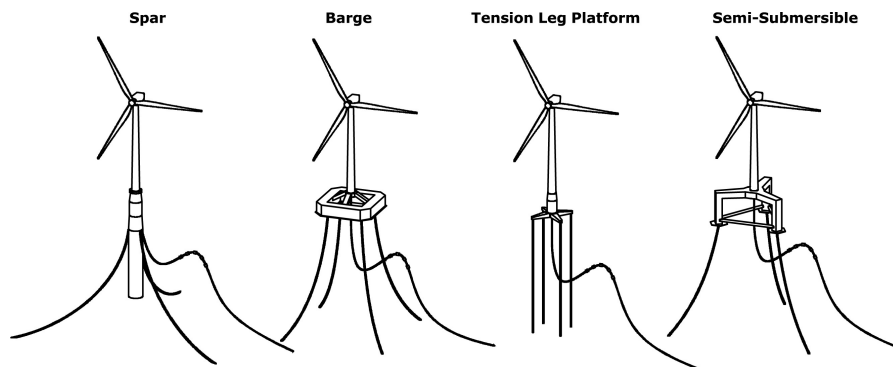


Figure 1.1: Floating offshore wind turbine support structure types. [3]

Among the types of floating support structures, TLPs present better dynamic properties in harsh environmental conditions due to their minimal pitch (i.e. rotational motion of a floating structure around

its transverse axis) and heave (i.e. vertical motion of a floating structure) responses [4]. Furthermore, they have a limited footprint on the sea bottom [5], which is preferable for the marine environment.

TLPs are subject to cyclic environmental loads, which can lead to fatigue. In offshore structures, fatigue is a significant failure mode [6, 7]. During the design phase of structures, calculations to predict the fatigue lifetime are performed. However, there is a high number of uncertainties related to the environmental loads the structure encounters [8]. Monitoring of the structural response (at fatigue hot spots) can enable the assessment of the remaining lifetime of the structure together with the verification of the design [9].

1.1.2. Structural Health Monitoring for Fatigue in Offshore Structures

Structural Health Monitoring (SHM) is a multidisciplinary process that involves the continuous or periodic collection and analysis of data from sensors integrated into the structures to assess the structural integrity and performance throughout their lifetime. SHM is widely applied in civil, aerospace, mechanical and offshore industries to predict and/or identify damage in the structure and/or verify the design [10]. SHM is important for offshore structures due to the uncertain environmental loads they encounter.

Prediction or early detection of damage in an OWT can be useful for maintenance. Continuous inspections are not feasible for offshore structures due to their high costs and the challenges involved (e.g. harsh environmental conditions, accessibility and safety of personnel) [11]. SHM facilitates the optimization of inspection activities and repair procedures [12]. It can also help reduce Operation and Maintenance (O&M) costs, which is a relevant contributor to the Levelized Cost of Energy (LCoE) (i.e. average cost of generating electricity per unit of energy produced) for OWTs [13–15]. SHM plays a part in reducing costs of maintenance (part of O&M) due to early detection of damage (allowing for timely intervention which prevents severe failures with costly repairs) and optimization of inspection activities (reducing unnecessary interventions and associated costs).

Fatigue monitoring can be beneficial for structures, especially in challenging environments such as offshore applications like TLPs. Given the substantial uncertainties associated with environmental loads, continuous monitoring of the structural response time histories at fatigue hot spots is crucial to accurately estimate the remaining lifetime of the structure in real-time [9]. This real-time assessment can optimize maintenance planning and can prevent unexpected failures [16]. However, direct measurement of these hot spots is often impractical due to issues including limited accessibility and high strain gradients. SHM systems employ sensor-based technology. These sensors can continuously monitor the structure's condition, capturing data that reflects the structure's health. Processing and analyzing this data can enable to gain insights into the structure's fatigue state [9].

1.2. Preliminary Knowledge

1.2.1. Tension Leg Platform

1.2.1.1. Description

A Tension Leg Platform (TLP) is a type of offshore floating support structure of various marine installations through tensioned vertical tendons. The principal component of a TLP is the hull, which consists of one or multiple columns. The TLP model of Bluewater Energy Services (BES) has one column with horizontal pontoons connected at the bottom of this column. The hull can have several functions such as providing buoyancy for the structure, tension for the tendons of the mooring system, and support for the wind turbine. The TLP hull also provides storage for marine systems. A conventional TLP hull used in the offshore Oil and Gas (O&G) industry can have circular columns (with the aim of lowering the drag loads) and rectangular pontoons [17]. The BES TLP design (Figure 1.2) has these characteristics.

TLPs are moored to the seabed by means of a mooring system. Tendons (i.e. vertical tension elements that have significant axial stiffness) are the main component of the mooring system. Each pontoon can have one or multiple tendons, and these are attached at the end of the pontoon. Steel wires are employed as tendons in the BES TLP model.

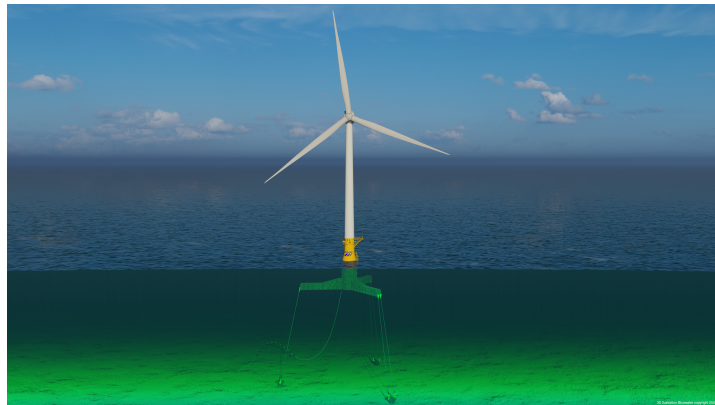


Figure 1.2: Floating Offshore Wind Tension Leg Platform from Bluewater. [18]

1.2.1.2. Mechanics

TLPs are floating support structures vertically moored by tendons. The tendons can be pre-tensioned by hull buoyancy and they need to be maintained in tension in operating conditions. The tension also provides the structure with horizontal restoring force in the circumstance that it shifts horizontally, leading to no requirement for a horizontal mooring system [19]. This fact can be appreciated in Figure 1.3 for a multi-column model with F_T as the tension force and F_H as the horizontal restoring force. Another possible function of the tendons is to give the entire structure stability.

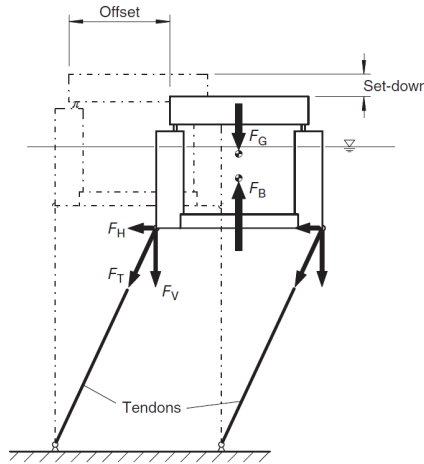


Figure 1.3: Forces on a TLP in an offset position. [19]

TLPs have short natural periods for the vertical modes (i.e. heave, pitch, and roll) due to the high axial stiffness of tendons, while they have longer natural periods for horizontal modes (surge, sway, and yaw). Resonant vibrations, such as Vortex-Induced Vibrations (VIV) and wind-induced vibrations (e.g., 3P, 6P, and 9P resonances from the wind turbine), can occur in the case of FOWTs [19].

There are other dynamic phenomena for TLPs to consider. Ringing is strong vertical vibrations under severe loading and springing is the vertical response due to second-order wave effects [20]. Wave-frequency responses are oscillatory motions close to incident wave frequencies and slow-drift motions are low-frequency lateral oscillations [21]. Vortex Induced Motions (VIM) (caused by vortex shedding behind columns) lead to oscillating lift and drag forces that result in increased fatigue damage in the tendons and higher mooring loads [22, 23].

1.2.1.3. Failure

Awareness of possible failure modes and their causes can be beneficial for this type of offshore structure situated in remote locations. This knowledge can help the risk of unexpected failures. According to Kang et al. [24], the support structure for FOWT's failures occur at the flange bolt and weld area as a consequence of fatigue. Offshore structures are subjected to cyclic loads from environmental conditions, which can induce fatigue damage accumulation. The fatigue assessment is more challenging for floating support structures rather than for bottom-fixed. This is a consequence of wind generating global motions that will lead to forces and stresses in the structure [25]. This fact suggests the need to monitor fatigue in the support structure.

1.2.1.4. Critical Locations

The most critical locations, especially for fatigue, are generally considered the connections between structural components (since loads are transferred through those connections). These loads produce stress, which concentrates in locations with geometry variation, inducing cracks and leading to fatigue failure. In the case of TLPs for wind turbines, the main connection is the one between the pontoons and the column, where there is a significant change of geometry. Another critical connection is present

between the platform and the tower of the turbine, although the variance in geometry is not that notable.

To identify the fatigue sensitive locations for the BES TLP model, the *Structural* section from Bluewater performed a fatigue analysis, as detailed in [Appendix A](#). This analysis showed that the locations with maximum damage utilization coincide with the assumption made previously. The maximum fatigue damage is found in the corners of the connections between the pontoons and the column due to the high bending loads of the pontoons and wind loads from the turbine. Moreover, the connection between the turbine tower and the TLP's column has generally more fatigue utilization than the rest of the structure, although not the maximum. Therefore, the two connections mentioned before are the critical locations that can be considered relevant to monitor with the SHM system.

1.2.2. Loads

Tension Leg Platform Wind Turbines (TLPWTs) are exposed to a variety of loading conditions determined by the environment, by the operation status, and possibly by accidents [26]. [Figure 1.4](#) illustrates multiple load sources for FOWTs.

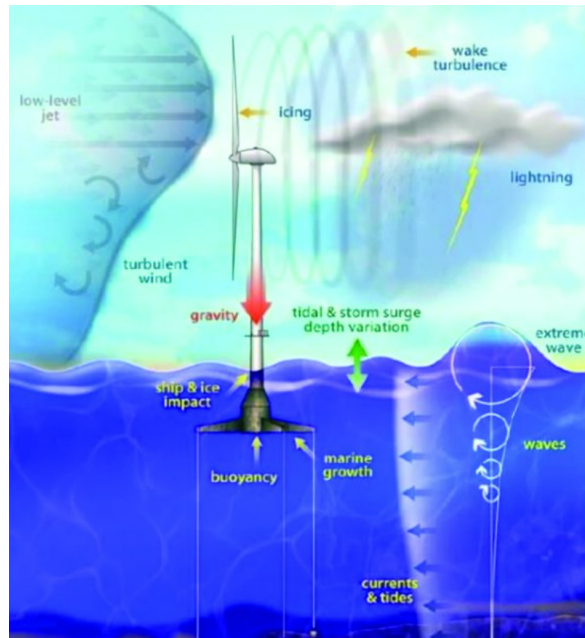


Figure 1.4: Load sources of FOWTs. [27]

1.2.2.1. Environmental Loads

Hydro loads are generated by the sea. These loads can have static or dynamic nature. The latter kind is considered to be one of the most challenging loads according to Yu [28]. Within the hydrodynamic forces, there are loads that can be induced by current and tides, waves, and their combination. The forces created by the current are typically referred to as drag and lift [29].

The static loads generated by the sea are the hydrostatic pressure and buoyancy. Hydrostatic pressure can be defined as the pressure distribution of a fluid at rest [30]. According to Archimedes' principle,

an object's buoyancy is determined by an upward force that is equivalent to the weight of the fluid displaced [31].

Regarding the hydrodynamic loads generated by waves, there are various hydrodynamic theories to consider. First-order potential flow theory accurately models wave excitation, including Froude-Krylov and diffraction effects, in large volume structures. Radiation and diffraction pressures, as well as added mass and radiation damping coefficients, can be obtained from this theory [32]. Second-order potential flow theory is relevant for low-frequency surge motions and high-frequency pitch or heave springing responses in FOWTs. Third-order potential flow theory approximations are used for computing ringing responses in large and steep waves. Viscous damping can be calculated using Morison's equation with appropriate coefficients for large volume structures. In dynamic analysis, Morison's equation is used for slender elements and potential theory formulation for large volume bodies [26].

The aerodynamic forces generated by wind loads on the turbine tower can induce dynamic behaviour on the FOWT, including roll and pitch motions. These motions can lead to bending moments in the tower, which translate into stresses in the TLP.

1.2.2.2. Mooring loads

The pretension of the mooring lines is needed to provide the structure with stability and station keeping. According to DNV-ST-0119 [25], this pretension of tendons is considered a permanent load for a sea-state, which means that they do not vary in magnitude, position, or direction during the considered time.

With respect to dynamic loads coming from the mooring lines, offshore marine structures with small structural periods are sensitive to high-frequency loads, which can provoke high transient effects or resonant responses. These responses can generate ringing or springing [33]. The first one can come with extreme sea conditions and it is considered a transient event, while the latter one takes place in steady-states [25]. These are identified to increase the tendon loads [34], as well as VIM [23], which affect the structural integrity of the TLP hull.

1.3. Literature Review

Fatigue is a major failure mechanism for these structures. Fatigue monitoring in offshore structures can contribute to evaluating the remaining lifetime of the structure in real time.

In fatigue monitoring, knowledge of stress histories at locations prone to fatigue (i.e. hot spots) is essential to accurately assess fatigue in the structure. However, it is not feasible to directly monitor these locations as they have a high gradient strain field (affecting the accuracy of the measurements), they experience large deformations (which would be critical for the physical integrity of sensors) and a considerable number of sensors would be required. Force identification and/or response estimation are typically employed to perform fatigue monitoring [9].

1.3.1. Force Identification

For fatigue assessment, when the stress history of the hot spot is not available, an alternative is to perform the prediction of the remaining lifetime using the time history of external forces. In numerous situations, measurement of the external loads is complicated or not possible because of sensor limitations or the unknown origin of the forces, so an estimation of the forces may be done. The force identification approach enables the reconstruction of the time history of external forces using indirect measurement techniques. These techniques can be transformations of measured parameters like velocity, acceleration, strain, position, or Supervisory Control and Data Acquisition (SCADA) [35].

Different force identification algorithms have been suggested in the existing literature [35–38]. In addition, various Kalman filter-based force identification techniques have been also proposed in the literature [39–43].

The Monitas System is an Advisory Monitoring System (AMS) to control the fatigue lifetime consumption of FPSO hulls. This system was developed for the Glas DOWRS Floating Production Storage and Offloading (FPSO) of Bluewater within the Monitas Joint Industry Project (JIP). This system obtains information about the fatigue lifetime consumption from the fatigue design data, fatigue design tool, and the monitoring data of hull girder loads, global and local stresses, wave frequency motions, the ship's loading condition and heading, and the environmental conditions [44]. Hageman [8] investigated the uncertainties in the stresses that generate fatigue accumulation.

1.3.2. Response Estimation or Virtual Sensing

Virtual sensing can enable full-field stress and/or strain estimation from a limited set of measurements. It allows precise strain estimation in fatigue hot spots without the necessity of installing sensors directly in those specific locations [45].

Virtual sensing can be classified into probabilistic state estimation and deterministic model-based extrapolation. The most used approaches for them are the Kalman filter and Modal Decomposition and Expansion (MDE), respectively. Due to their extensive use, they are explored.

1.3.2.1. Kalman Filter

For probabilistic state estimation, the response states are considered as random variables and the measured data is used to estimate their probability distributions.

A Kalman filter is an algorithm to estimate the state of a stochastic system [46] while minimizing the Mean Squared Error (MSE). It is common to use it for virtual sensing in strain or stress prediction for the fatigue assessment of structures [9, 39, 47–51]. Figure 1.5 represents the process of the fatigue lifetime prediction in an entire structure from a limited number of physical sensors using Kalman filter, where n number of measured points are denoted by S_n and m number of predicted points by P_m .

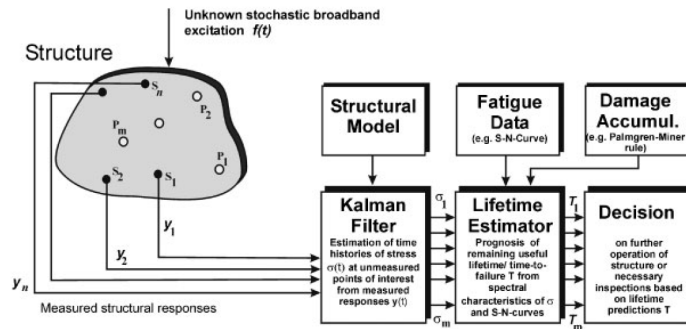


Figure 1.5: Scheme of fatigue lifetime prediction from a limited number of sensors using a Kalman filter-based algorithm. [47]

1.3.2.2. MDE

MDE is a widely-used technique in the field of structural dynamics and vibration analysis, particularly for systems that exhibit complex dynamic behaviour, such as offshore wind turbines, bridges, and aircraft structures. In the context of structural dynamics, deterministic model-based extrapolation relies on physics-based models to predict the behaviour of a structure under different loading conditions. These models typically use simplified assumptions about material properties, geometry, and boundary conditions to represent the structure's behaviour [45].

This method relies on the expansion from a limited set of measurements to the full-field response. The expansion is performed based on the mode shapes of the structure. Measurements can be strains or accelerations, usually obtained with strain gauges and accelerometers. Researchers classify this approach into two categories: those that rely on Finite Element (FE) mode shapes, and those that utilize expanded experimental mode shapes [45].

FE Mode Shapes

One way to evaluate the mode shapes over the assessed structure is to extract them from a FE model. However, they also imply the risk of modeling errors [52].

Iliopoulos et al. [53–55] applied a multi-band modal expansion approach on a monopile OWT. The researchers considered the quasi-static and dynamic loads to perform the reconstruction of the full-field response. This was achieved using a limited number of accelerometers and strain sensors together with a calibrated FE model. It was concluded that this method was successful to predict the full-field strains as well as the strain histories at fatigue hot spots. Utilizing various frequency bands proved to be an effective strategy to mitigate the challenges associated with estimating the response spectrum in higher frequency regions [9]. A schematic representation of this methodology, especially for this type of structure, is shown in Figure 1.6.

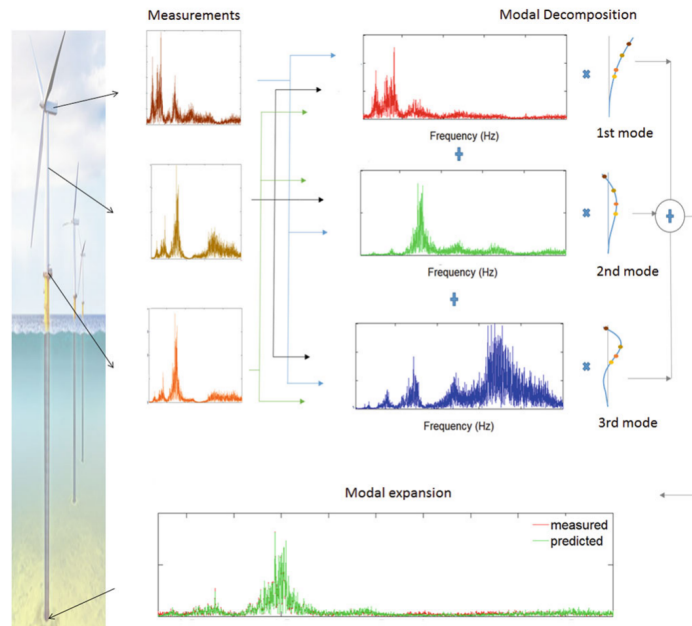


Figure 1.6: MDE in a schematic representation for the case of a OWT. [54]

Sireta et al. [56] presented a method for fatigue damage and extreme stress prediction using 8 strain gauges and a 3D FE model of the ship's hull. This method is based on previous works which use a conversion matrix and a linear decomposition of the structural response based on the selected modes. The method was validated numerically. The error levels were found to be 1-20% on maximum stresses and 3-80% on fatigue damage depending on the locations. These results were obtained with an existing sensor layout. They are expected to improve if this layout is optimized for this methodology.

In a more general case study, Bogert et al. [57] applied MDE to reconstruct the deformed shape of a loaded cantilever aluminum plate. The authors used strain measurements together with the modal matrices calculated from a FE model. The plate was subjected to loading that generated bending, torsion, shear, and in-plane deformations. The reconstruction reflected close correspondence with measurements from a laboratory. They also proposed modal selection procedures to identify the most important structural modes.

Experimental Mode Shapes

Alternatively to the previous approach, experimental modes can be extracted from operational modal analysis (OMA) [52].

Hjelm et al. [58] demonstrated that stress histories can be accurately estimated by integrating measured accelerations to obtain displacements. The researchers used MDE with experimental mode shapes. The method was tested in two structures with two different experiments. One was performed in a cantilever beam with a mounted beam and weight on the top, and another one on a lattice tower. The results from the latter one (with stochastic loading) showed a low Coefficient of Variation (COV) on the stress history (below 0.05).

Henkel et al. [59] applied a dual-band MDE to jacket substructures for OWTs to monitor the fatigue progression in the critical welds. Using this type of MDE, the spectrum of turbine loads is split into frequency bands (a quasi-static and a dynamic one). The results showed high accuracy (with relative errors on the damage equivalent load (DEL) smaller than 25%) for the prediction of fatigue progress on leg welds of K-joints with most of the considered load cases. However, there are challenges in predicting fatigue in X-joints due to the presence of local modes and limitations in extrapolating wave loading. The research also revealed a decrease in accuracy when dealing with load conditions with severe sea states.

Tarpø et al. [60] explored the accuracy of stress prediction from operational responses in their research study. The experimental mode shapes are expanded using a FE model. Then, an experimental test on a scaled tripod platform showed encouraging results and the strain history was predicted with high accuracy. More studies were performed with experimental mode shapes [52, 61–63].

In their work, Tarpø et al. [45] compared the utilization of both mode shapes from a FE model and expanded experimental mode shapes. Figure 1.7 illustrates the process of mode shape expansion for OMA. The study revealed that the latter can improve the precision of stress estimation. Expanding experimental mode shapes with a FE model holds the potential to diminish the modeling errors inherent in the FE model. However, the expansion process itself is a fitting procedure that may induce fitting errors; so it must be employed carefully.

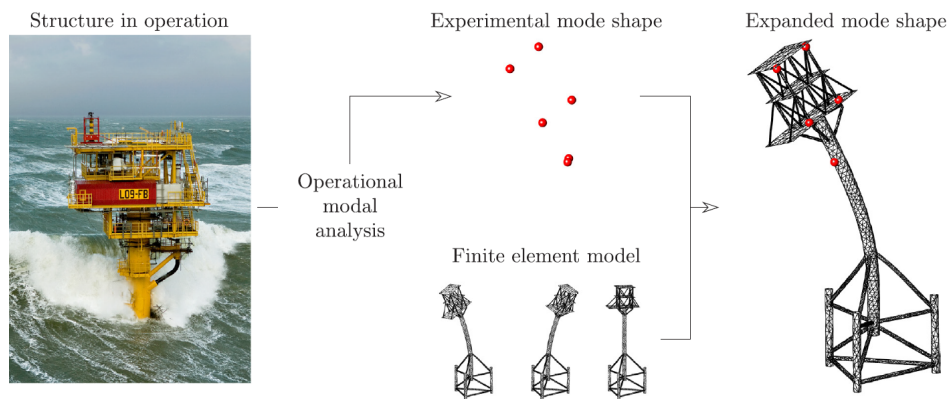


Figure 1.7: Illustration of mode shape expansion [45]

1.3.2.3. Comparison between MDE and Kalman Filter

To compare deterministic extrapolation and probabilistic state estimation, Maes et al. [9] performed the estimation of dynamic strains for the fatigue assessment of an OWT. The authors used Kalman filtering, joint input-state estimation, and modal expansion (with modal shapes from a FE model) algorithms. It was concluded that all methods provide accurate results. Moreover, Ren and Zhou [49] investigated the accuracy and efficiency of the Kalman filter and the modal expansion algorithms for strain estimation of a steel truss bridge. It was demonstrated that both algorithms showed encouraging

results. The time and frequency domain estimated response closely aligned with the simulated data from the truss structure, which contained noisy contamination and white noise.

1.3.3. Literature Review Conclusions

Response estimation can be beneficial for both fatigue assessment of the structure and verification of the design without the need of estimating the loads. By predicting the stress histories in the fatigue prone locations, the remaining fatigue lifetime can be estimated. This can be helpful for advising the operator (e.g. to optimize the maintenance plan). The reconstruction of the structural behavior provides as well a means to verify that the structure is performing as intended according to design specifications. MDE offers an efficient approach to accurately perform the full-field stress/strain estimation. TLPs supporting FOWTs have complex dynamic behaviour due to the hydrodynamic loads affecting the TLP and the aerodynamic loads on the turbine tower. MDE has the potential to capture this dynamic behaviour and estimate the structural response as the reconstruction process relies on modal parameters. To predict the structural response, Kalman filter-based approaches produced promising results for monopile-type support structures. However, TLPs are more complex, so calibration of the model done with MDE (not possible with the Kalman filter) is valuable.

1.4. Knowledge Gap and Research Direction

1.4.1. Knowledge Gap

A knowledge gap has been revealed to exist concerning the SHM of TLPs supporting FOWTs. Because it is a relatively new floating support structure for OWTs, research conducted about monitoring fatigue in an efficient way is limited. In this research, MDE has been selected for the design of a fatigue monitoring system for these structures.

1.4.2. Research Direction

The knowledge gap highlights the need for further research in fatigue monitoring of TLP support structures for FOWTs.

This investigation aims to address the identified knowledge gap. It will contribute to the understanding of TLP behaviour under complex and unknown loading conditions. This will be achieved by developing an efficient fatigue monitoring system.

This research can be pursued by attempting to answer the following main research question:

What are the required characteristics of a fatigue monitoring system using MDE for a TLP supporting a FOWT?

From the principal research question, several sub-questions arise that will help guide the investigation and answer it:

- Is the application of MDE suitable for reconstructing the structural response of a TLP supporting a FOWT?
- How sensitive is MDE for the fatigue monitoring of a simple structure (e.g. cantilever beam) to the measurement error, unexpected loading conditions, and different amounts of modes and/or sensors?
- What is the optimal sensor layout for the monitoring system?
- How sensitive is the monitoring system to the mass distribution, measurement error, or unexpected loading conditions?

1.5. Report Outline and Collaboration Partner

1.5.1. Report Outline

The report has the following structure. Chapter 1 presents the motivation, preliminary knowledge, literature review, and research direction. Chapter 2 describes the mathematical framework used in this study along with the approach followed. Chapter 3 discusses the analysis performed and the results obtained. Chapter 4 presents the design of the fatigue monitoring system with the modal selection and the sensor layout. Chapter 5 discusses the sensitivity analysis performed to explore the limitations of the monitoring system. Chapter 6 discusses the conclusions of the study and presents future recommendations.

1.5.2. Collaboration Partner

Bluewater Energy Services (BES) is a company founded in 1987. It designs, owns and operates several ships and offshore structures such as Floating Production Storage and Offloading (FPSO) units. Since 2006 Bluewater develops technology for renewable offshore energy. Bluewater offers a TLP as the solution for support structures for FOWTs.

This MSc Thesis is performed in collaboration with Bluewater, specifically the *Naval & Marine* and *Structural* sections from the *Engineering* Department. The BES TLP model will be the model of use for this Graduation Project as basis.

2

Methodology

2.1. Mathematical framework

2.1.1. Modal Decomposition

The Equation Of Motion (EOM) governing the displacement $\mathbf{u}(t)$ of a linear system (discretized in the space domain) subject to a dynamic load can be expressed as [9, 45, 64, 65]:

$$\mathbf{M}\ddot{\mathbf{u}}(t) + \mathbf{C}\dot{\mathbf{u}}(t) + \mathbf{K}\mathbf{u}(t) = \mathbf{f}(t) \quad (2.1)$$

where $\mathbf{u}(t) \in \mathbb{R}^N$ is the displacement, $\dot{\mathbf{u}}(t) \in \mathbb{R}^N$ is the velocity and $\ddot{\mathbf{u}}(t) \in \mathbb{R}^N$ is the acceleration vector respectively. N is the number of degrees of freedom (DOFs). $\mathbf{M} \in \mathbb{R}^{N \times N}$, $\mathbf{C} \in \mathbb{R}^{N \times N}$ and $\mathbf{K} \in \mathbb{R}^{N \times N}$ are the mass, damping, and stiffness matrices respectively, and $\mathbf{f}(t) \in \mathbb{R}^N$ is the external force vector.

With the assumption of small damping and no external excitation (i.e. free vibration), the EOM (Equation 2.1) describing the free vibration of an undamped system can be rewritten as:

$$\mathbf{M}\ddot{\mathbf{u}}(t) + \mathbf{K}\mathbf{u}(t) = \mathbf{0} \quad (2.2)$$

Considering an arbitrary natural vibration mode i of the system considered, the displacement $\mathbf{u}(t)$ can be described in terms of the modes shapes by:

$$\mathbf{u}(t) = \boldsymbol{\phi}_i \cdot q_i(t) \quad (2.3)$$

where the modal coordinate $q_i(t)$ for the i^{th} mode can be described by the harmonic function:

$$q_i(t) = A_i \cos(\omega_i t) + B_i \sin(\omega_i t) \quad (2.4)$$

where A_i and B_i are constants determined by the initial conditions and ω_i is the natural frequency for the i^{th} mode.

Substituting Equation 2.4 into Equation 2.3 and performing the second time derivative of $\mathbf{u}(t)$, displacement and acceleration, respectively, results in:

$$\mathbf{u}(t) = \boldsymbol{\phi}_i \cdot \left(A_i \cos(\omega_i t) + B_i \sin(\omega_i t) \right) \quad (2.5)$$

$$\ddot{\mathbf{u}}(t) = -\boldsymbol{\phi}_i \cdot \omega_i^2 \cdot \left(A_i \cos(\omega_i t) + B_i \sin(\omega_i t) \right) \quad (2.6)$$

Introducing Equation 2.5 and Equation 2.6 into the undamped equation of motion (Equation 2.2), the eigenvalue problem to compute the mode shapes and the natural frequencies is obtained:

$$\mathbf{M} \left(-\boldsymbol{\phi}_i \cdot \omega_{n,i}^2 \cdot (A_i \cos(\omega_i t) + B_i \sin(\omega_i t)) \right) + \mathbf{K} \left(\boldsymbol{\phi}_i \cdot (A_i \cos(\omega_i t) + B_i \sin(\omega_i t)) \right) = \mathbf{0} \quad (2.7)$$

$$\omega_i^2 \mathbf{M} \boldsymbol{\phi}_i = \mathbf{K} \boldsymbol{\phi}_i \quad (2.8)$$

where ω_i and $\boldsymbol{\phi}_i$ are eigenvalue and eigenvector, respectively for the i^{th} mode. The modal matrix (containing all modes as column vectors) is $\boldsymbol{\Phi} = [\boldsymbol{\phi}_1, \dots, \boldsymbol{\phi}_N]$, where $\boldsymbol{\Phi} \in \mathbb{R}^{N \times N}$. The response of a structure is located in a vector space $S(\boldsymbol{\Phi})$ spanned by all modes.

Using the modal decomposition approach [66–68], the displacement vector $\mathbf{u}(t)$ can be expressed as a linear combination of the mode shapes:

$$\mathbf{u}(t) = \sum_{i=1}^N \boldsymbol{\phi}_i q_i(t) \quad (2.9)$$

The total number of DOFs N is composed of two subsets. One consists of the measured DOFs with physical sensors (also called active DOFs) and the other contains the predicted DOFs (inactive DOFs), which correspond to the virtual sensors. The two subsets are denoted with the subscripts m and p , respectively. The same can be done with the modal matrix. Thus:

$$\mathbf{u}(t) = \begin{bmatrix} \mathbf{u}_m(t) \\ \mathbf{u}_p(t) \end{bmatrix}, \quad \boldsymbol{\Phi} = \begin{bmatrix} \boldsymbol{\Phi}_m \\ \boldsymbol{\Phi}_p \end{bmatrix} \quad (2.10)$$

where the displacement vector for measured DOFs is $\mathbf{u}_m(t) \in \mathbb{R}^{N_m}$ and the predicted DOFs is $\mathbf{u}_p(t) \in \mathbb{R}^{N_p}$. N_m are the number of measured DOFs and N_p is the number of predicted DOFs. The spatial limitation is also applied for the modal matrix, where the matrices for the measured and predicted DOFs are, respectively, $\boldsymbol{\Phi}_m \in \mathbb{R}^{N_m \times N}$ and $\boldsymbol{\Phi}_p \in \mathbb{R}^{N_p \times N}$.

In order to limit the number of modes, modal truncation can be performed. This is because the original number of modes is too high for a regular FE model and it can have consequences in computational time. An approach suggested by Mršnik et al [56] is to select only the most representative modes, usually by truncating the high-frequency modes because their contribution to the response can be considered negligible. Then, being M the number of modes considered, the truncated and estimated modal matrix is $\hat{\boldsymbol{\Phi}} \in \mathbb{R}^{N \times M}$, and the linear subspace (where the estimated response is situated) becomes $\hat{S}(\hat{\boldsymbol{\Phi}})$ (an approximation of $S(\boldsymbol{\Phi})$).

The subsets of the estimated displacement vector and the modal matrix can be estimated:

$$\hat{\mathbf{u}}(t) = \begin{bmatrix} \mathbf{u}_m(t) \\ \hat{\mathbf{u}}_p(t) \end{bmatrix}, \quad \hat{\boldsymbol{\Phi}} = \begin{bmatrix} \hat{\boldsymbol{\Phi}}_m \\ \hat{\boldsymbol{\Phi}}_p \end{bmatrix} \quad (2.11)$$

where the estimated displacement vector and estimated modal matrix for the predicted DOFs are $\hat{\mathbf{u}}_p(t) \in \mathbb{R}^{N_p}$ and $\hat{\boldsymbol{\Phi}}_p \in \mathbb{R}^{N_p \times M}$. The measured displacement vector and estimated modal matrix for the measured DOFs are $\hat{\mathbf{u}}_m(t) \in \mathbb{R}^{N_m}$ and $\hat{\boldsymbol{\Phi}}_m \in \mathbb{R}^{N_m \times M}$.

2.1.2. Modal Expansion

Recalling [Equation 2.9](#), the estimated displacement response can be then written as follows:

$$\hat{\mathbf{u}}(t) = \hat{\mathbf{\Phi}}\hat{\mathbf{q}}(t) \quad (2.12)$$

The estimated modal coordinates can be computed using the estimated displacements and the modal matrix for the measured DOFs:

$$\hat{\mathbf{q}}(t) = (\hat{\mathbf{\Phi}}_m^T \hat{\mathbf{\Phi}}_m)^{-1} \hat{\mathbf{\Phi}}_m^T \hat{\mathbf{u}}_m(t) = \hat{\mathbf{\Phi}}_m^\dagger \mathbf{u}_m(t) \quad (2.13)$$

where $[\bullet]^\dagger$ is the Moore-Penrose pseudo-inverse. It is described by Moore [\[69\]](#), Bjerhammar and Penrose [\[70\]](#).

The expansion of the measurements to the full-field displacement can now be performed using using [Equation 2.12](#) [\[45, 53–55, 59, 63, 71\]](#). The same relation can be established in terms of strain since the measured data considered in this project is strain. The estimated strain is computed with the modal coordinates obtained in [Equation 2.13](#) since they are the same for displacement and strain [\[72\]](#):

$$\hat{\boldsymbol{\epsilon}}(t) = \hat{\mathbf{\Phi}}_\epsilon \hat{\mathbf{q}}(t) \quad (2.14)$$

where $\hat{\mathbf{\Phi}}_\epsilon$ is the modal matrix in terms of strain instead of displacements, and it can be extracted from the FE model [\[45, 73\]](#).

[Equation 2.14](#) can be rewritten in terms of the measured strains, which would be transformed from the measured strains using the same approach as for the displacements.

$$\hat{\boldsymbol{\epsilon}}(t) = \hat{\mathbf{\Phi}}_\epsilon \hat{\mathbf{\Phi}}_{\epsilon,m}^\dagger \boldsymbol{\epsilon}_m(t) \quad (2.15)$$

Then, the estimated full-field strains can be transformed into stresses with the constitutive equation using Hooke's law [\[74\]](#):

$$\boldsymbol{\sigma} = E\boldsymbol{\epsilon} \quad (2.16)$$

where E is the Young's modulus.

For the fatigue assessment, the hot-spot stresses are computed by applying the FE relationship between the far-field stresses and the hot-spot stresses [\[71\]](#).

The validity of the methodology is confirmed through its application to a simpler structure (i.e. a cantilever beam), which can be found in [Appendix B](#).

2.2. Approach

Accelerometers are suitable for measuring medium-high frequencies. Usually, they can perform accurate measurements with frequency ranges starting from 10 or 50 Hz [\[75, 76\]](#). FOWT generally have responses

with frequencies up to 1.5 Hz, approximately [77]. Strain gauges can be an appropriate option for the design of a fatigue monitoring system for TLPs supporting FOWTs.

Due to a lack of experimental data, simulations are used to generate a representative database. Strain mode shapes generated from a FE model are employed.

This research is conducted by following the subsequent steps:

- **Application of MDE to a simple structure (cantilever beam):** Initially, the MDE method is applied to a simple structure, such as a cantilever beam. This serves as a baseline to understand the implementation of the method and evaluate its performance under simple loading conditions. Then, a sensitivity analysis is conducted to study the influence of different parameters on the accuracy of the MDE method. This helps to identify critical factors that might affect the performance of the MDE method when applied to more complex structures. The analysis considers aspects such as measurement error, unexpected loading conditions, varying boundary conditions, and different amounts of modes and/or sensors. The application of MDE to a cantilever beam can be found in [Appendix B](#).
- **Application of MDE to the TLP:** After gaining insights from the application of MDE to the cantilever beam, the method is applied to the TLP supporting the FOWT. It starts with a simple model of the TLP without the turbine or tendons, and later the study is applied to a FOWT model. This involves choosing the most representative mode shapes to generate the modal matrix, which is used to estimate the dynamic response of the TLP under various loading conditions. After it, a similar sensitivity analysis on the cantilever beam is conducted for the TLP models to assess the impact of different parameters on the accuracy of the MDE method. This helps in refining the implementation of the method for the TLP and identifying potential challenges and limitations.
- **Design of the SHM system:** Building on the insights and findings from the previous steps, the final phase of the study involves the design of a fatigue SHM system for TLPs supporting FOWTs. The SHM system with the sensor layout is optimized to provide reliable and accurate fatigue monitoring for the TLP.

3

Analysis and Results

3.1. Simplified TLP

3.1.1. Introduction and Objective

The main aim of this investigation is the assessment of the application of Modal Decomposition and Expansion (MDE) in reconstructing the structural response of more complex structures (in comparison with a cantilever beam, presented in [Appendix B](#)). For this, MDE is applied to a simple model of a TLP. This model does not contain the rest of the components of a FOWT, so the considered modes are the local TLP modes.

3.1.2. Model

The FE model used in this analysis is a simplified version of the TLP model developed by Bluewater. Several simplifications are made to align the model with the aim of the investigation. The model's overall size is reduced by a factor of 100 in comparison to the actual TLP model from Bluewater. There are some proportional relationships that remain consistent with the original model. Some examples of these are the proportional relationship between the (averaged) height and the width of the pontoons, or between the lengths of the column and the pontoons. To further simplify, the model adopts uniform cross-sections, diverging from the original TLP model's varying cross-sectional profiles. This allows for a decrease in computational complexity without significantly affecting the relevance of the results.

The FE model is composed of shell elements because the stress through the thickness is not relevant in this investigation. The top is clamped, simulating the connection with the tower of the turbine. The tendons are modeled by applying vertical forces (downwards) at the end of the pontoons. The element size is 1 mm, so it is fine enough to provide accurate results in thin parts of the structure (pontoons) without increasing unnecessarily the computational time. [Figure 3.1](#) shows the model.

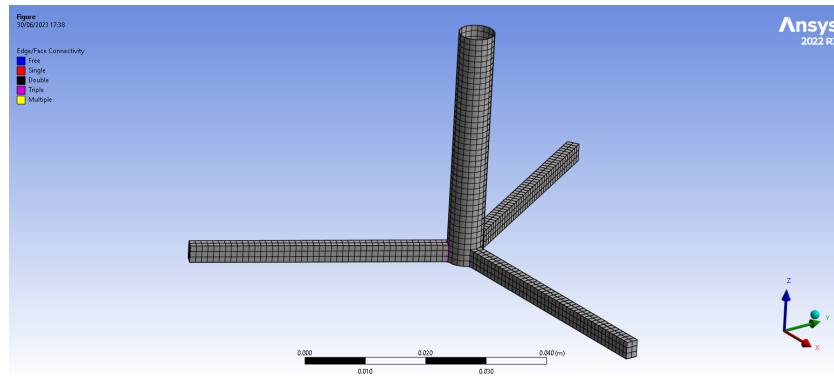


Figure 3.1: Simplified TLP FE model.

3.1.3. Results

3.1.3.1. Modal Matrix

In this analysis, the pontoons are investigated. The modal matrix in terms of strain for the modal expansion is generated as follows. A modal analysis is performed using Ansys Workbench. The modal selection is performed by observation. This approach involves choosing mode shapes that visually correspond to the structural behavior of the structure (i.e. modes that closely resemble the response). A modal selection approach will be developed for the FOWT model. The modal matrix is obtained by extracting the normal strain in the longitudinal direction of each pontoon for the selected modes.

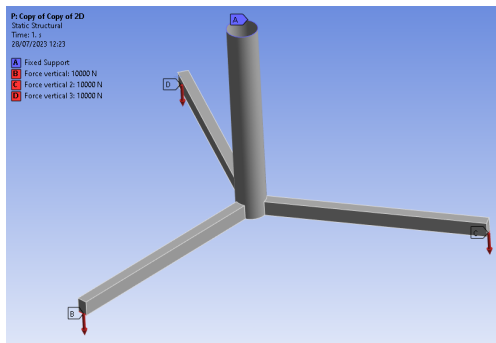
3.1.3.2. Numerical Response

The numerical structural response used in this investigation is static. This simulates a moment when a strain gauge takes a measurement. The static structural analysis is performed using Ansys Workbench.

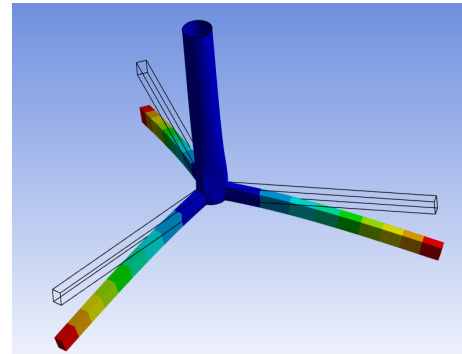
Different loading conditions are applied to observe the reconstruction in various situations.

Vertical Loads

One of the most significant loads that the TLP can experience is the vertical component of the tendon loads, pulling the end of the pontoons downwards. To model them, vertical loads at the end of the pontoons are applied. The boundary and loading conditions along with the structural response (total deformation) are illustrated in [Figure 3.2](#).



(a) Boundary and loading conditions.

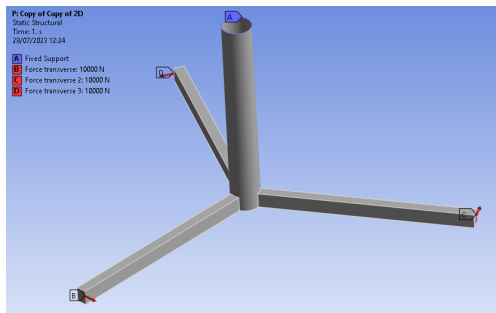


(b) Structural response.

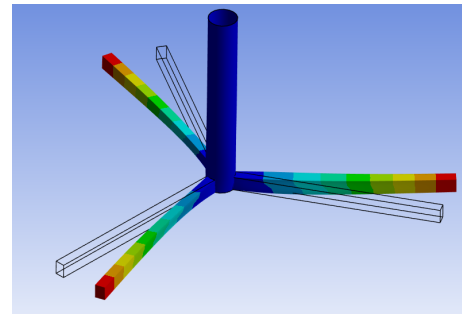
Figure 3.2: Model with vertical loads.

Transverse Loads

The TLP pontoons can experience transverse loads due to environmental loads (such as waves or current) or tendon loads. Transverse loads are applied to the end of the pontoons.



(a) Boundary and loading conditions.

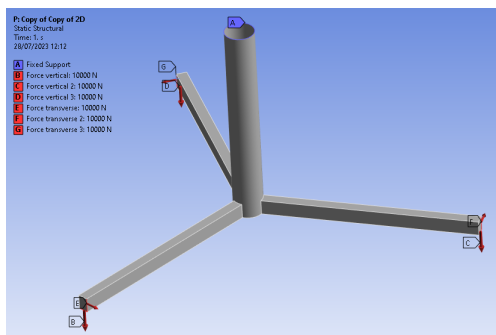


(b) Structural response.

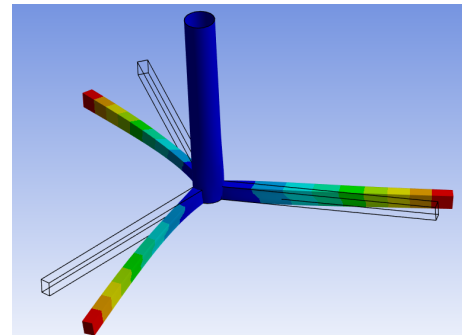
Figure 3.3: Model with transverse loads.

Combination

The previous loads can occur simultaneously. The vertical and transverse loads are applied to the model at the same time.



(a) Boundary and loading conditions.



(b) Structural response.

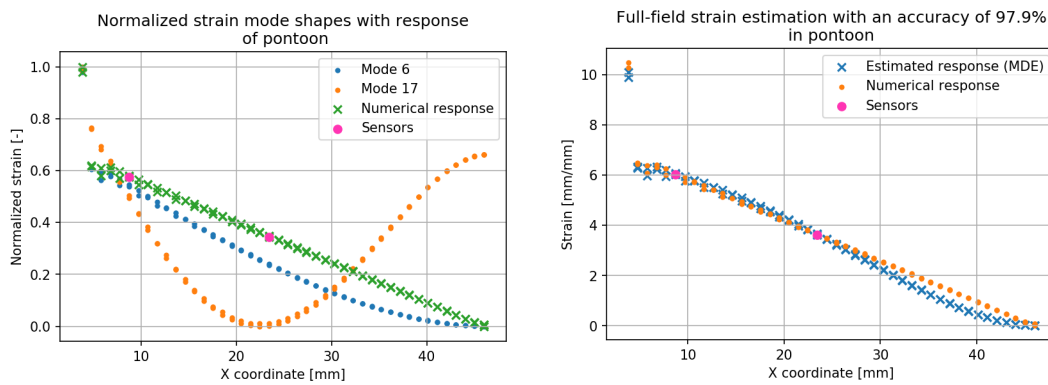
Figure 3.4: Model with combined loads.

3.1.3.3. Response Reconstruction

For all the case studies, 2 sensors and 2 modes are used. In this analysis, the sensor placement is performed by trying all possible sensor layouts and selecting the one that performs the reconstruction of the structural response with lower error. For the FOWT, a methodology to define the sensor placement is developed. The considered error for this selection is the mean relative error.

Vertical Loads in pontoons

The first 2 modes that have vertical bending in the pontoons are selected. Figure 3.7 show the normalized strain mode shapes along with the normalized numerical response (left) and the reconstruction of this response using the 2 mode shapes and the best sensor layout possible (right).



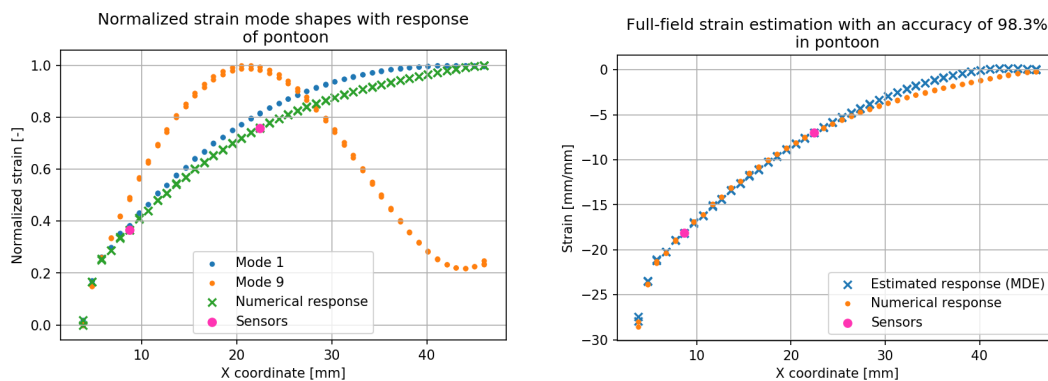
(a) Mode shapes with numerical response and best sensor layout. (b) Full-field strain estimation.

Figure 3.5: Structural response reconstruction with selected modes and best sensor layout in pontoon for vertical loads.

The accuracy is defined as 100% minus the mean relative error.

Transverse Loads in pontoons

For this case the first 2 modes where the pontoons experience transverse bending are selected.

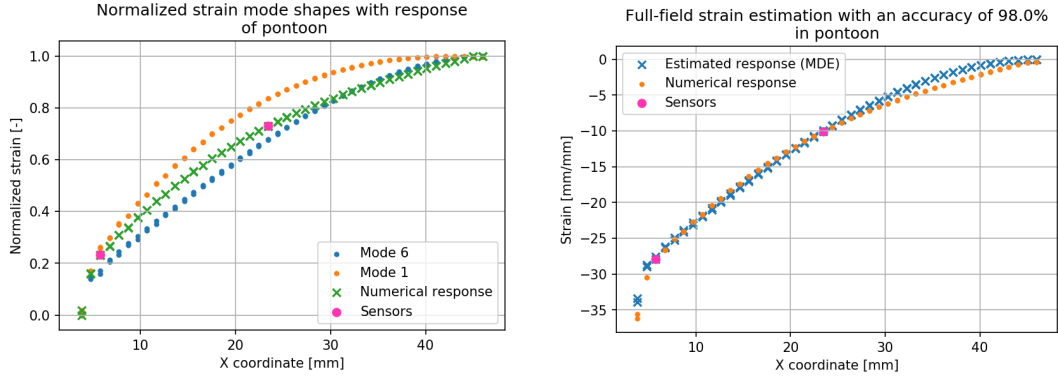


(a) Mode shapes with numerical response and best sensor layout. (b) Full-field strain estimation.

Figure 3.6: Structural response reconstruction with selected modes and best sensor layout in pontoon for transverse loads.

Combined Loads in pontoons

For the combined loads, the modal matrix is also a combination of the vertical and transverse ones. The first mode with vertical bending in the pontoons and the first one with transverse bending are selected.



(a) Mode shapes with numerical response and best sensor layout. (b) Full-field strain estimation.

Figure 3.7: Structural response reconstruction with selected modes and best sensor layout in pontoon for combined loads.

Vertical Loads in TLP

3.1.4. Conclusions

From this investigation, some conclusions can be drawn. The full-field strain in the pontoons of a TLP-like simple structure due bending can be accurately estimated using MDE. With 2 sensors in each pontoon, the reconstruction can have an accuracy of over 98%. Bending in different direction can be considered by selecting the correct mode shapes.

3.2. FOWT

3.2.1. Introduction and Objective

Puffin is a design and analysis tool developed by Bluewater. It integrates and automates the modelling, simulating, and assessing of designs of an offshore floating wind TLP. It generates two equivalent models, a static structural FE model of the TLP using Ansys Parametric Design Language (APDL) and a dynamic model of the FOWT with Orcaflex. The structural properties are calculated by Ansys and mapped to the dynamic model. Later, *Puffin* can instruct Orcaflex to run a dynamic simulation, from which the loads and accelerations are mapped back to the FE model to obtain the detailed structural response. With this response, the assessment of the performance of the design can be performed [78]. The dynamic model is used for this analysis.

The implementation of the MDE method to the FOWT dynamic model offers valuable analytical insights. The MDE method requires the global modes of the structure. This requirement is addressed by

the FOWT model. Orcaflex provides an accurate representation of the global modes as it takes into account the Fluid-Structure Interaction (FSI) effects. Accurately obtaining the global mode shapes of the entire FOWT structure is important for designing a fatigue monitoring system for a TLP supporting a FOWT using MDE.

3.2.2. Model

The numerical model of the FOWT used in this investigation is described in this section and it is shown in [Figure 3.8](#).

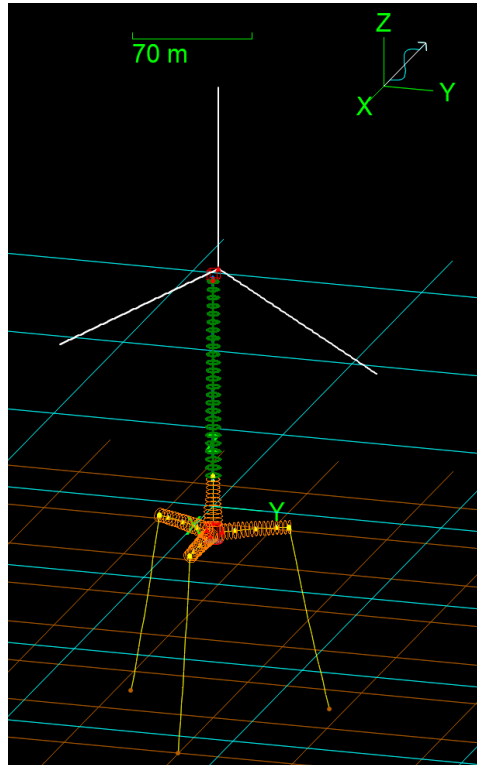


Figure 3.8: FOWT numerical model.

The model was calibrated and validated with model tests performed at the Maritime Research Institute Netherlands (MARIN) in January 2018 [79]. The calibration was executed by checking if the tension in the tendons of the model matched the tension from the model tests. This tension was computed from the balance between the total mass of the system and the displaced mass of the TLP [80].

3.2.2.1. Types of Elements

The model has three types of elements [81]:

- **Lines:** They are flexible linear elements represented by a lumped mass model. The line is modelled as a sequence of lumps of mass (nodes) connected by massless springs.
- **6D buoys:** They are rigid bodies with 6 DOFs. They have mass and moments of inertia, and forces and moments from different effects can be modelled.

- **3D buoys:** They are simplified point elements with 3 DOFs (only the translational DOFs). They do not have rotational properties, and moments acting on the buoy are disregarded.

3.2.2.2. Parts of the Model

The model is composed of 3 parts [80]:

- **Turbine:** The tower is modelled with line elements. The mass and stiffness properties are captured in the tower's model diameter and wall thickness. The nacelle and the rotor are modelled as point masses on top of the tower. The location of the masses in the longitudinal direction was slightly adjusted to better match the centre of gravity achieved by MARIN [79]. The properties of the tower, the nacelle and the rotor are based on the information from the wind turbine manufacturer HZ Wind [82]. The tower is 120 m.
- **TLP:** The column and the pontoons have non-constant cross-sections (with bulkheads, web frames and stiffeners). In Orcaflex, these properties are approximated by discretizing the line objects into various sections. The pontoons are modelled using line elements with a circular cross-section (not like the actual geometry). Each section has a diameter such that the volume of the section is equal to the volume of the actual pontoon over the same length range. The upper column of the TLP is the lower part of the tower of the turbine. It is modelled with line elements and a circular cross-section. The lower column of the TLP (i.e. the connection between the pontoons and the upper column) is modelled as a 6D buoy. It has a cylindrical shape with a given mass and inertia.
- **Mooring system:** In the model tests and the numerical model, the mooring system was simplified by using one tendon per pontoon (3 in total). The actual model has 2 tendons per pontoon (6 in total). The properties of the mooring lines are specified by MARIN [79].

3.2.2.3. Mesh

A convergence study is carried out to determine the size of the element. The parameter to determine the accuracy of the mesh is the maximum bending strain value in the pontoon aligned with the global X axis. This is because bending is governing in the pontoon. Figure 3.9 shows the convergence and adequacy of element length of 2.5 m.

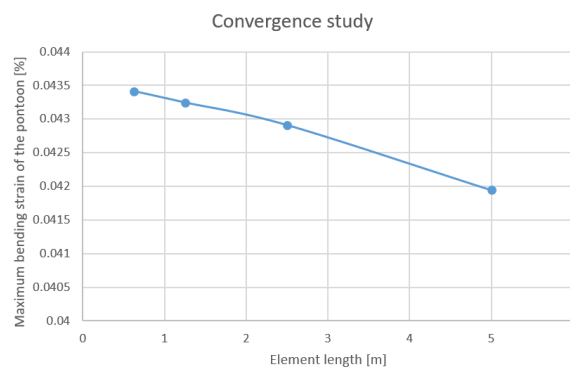


Figure 3.9: Convergence study for the mesh size.

3.2.2.4. Hydrodynamic Loads

The hydrodynamic loads affecting the structure are modelled using an extended form of Morison's equation. Originally, this equation was formulated by Morison et al. [83] (see Equation 3.1), to calculate the wave loads on fixed vertical cylinders. It has two force components: the fluid inertia force (related to water particle acceleration) and the drag force (related to water particle velocity). The original Morison's equation can be written as:

$$\mathbf{f} = \underbrace{C_m \Delta \mathbf{a}_f}_{\text{inertia}} + \underbrace{\frac{1}{2} \rho C_d A |\mathbf{v}_f| \mathbf{v}_f}_{\text{drag}} \quad (3.1)$$

where: \mathbf{f} = fluid force (per unit length) on the body

C_m = inertia coefficient for the body

Δ = mass of fluid displaced by the body

\mathbf{a}_f = fluid acceleration relative to earth

ρ = density of water

C_d = drag coefficient for the body

A = drag area

\mathbf{v}_f = fluid velocity relative to earth

The same principles can be applied to a moving body by incorporating adjustments. The inertia term is reduced by the amount $C_a \Delta \mathbf{a}_b$ and the drag term equation uses the body-relative velocity. The inertia force consists of two components: the Froude-Krylov and the added mass components. The former is due to the undisturbed pressure gradient and it is proportional to the fluid acceleration relative to earth \mathbf{a}_f . The latter is from the flow disturbance and it is proportional to the fluid acceleration relative to the body \mathbf{a}_r . The inertia coefficient C_m is taken to be $1 + C_a$ because the experimental coefficient of 1.0 for the Froude-Krylov is considered accurate [80]. The extended form of Morison's equation is used in OrcaFlex [81]:

$$\mathbf{f} = (\Delta \mathbf{a}_f - C_a \Delta \mathbf{a}_b) + \frac{1}{2} \rho C_d A |\mathbf{v}_r| \mathbf{v}_r \quad (3.2)$$

where: C_a = added mass coefficient for the body

\mathbf{a}_b = body acceleration relative to earth

\mathbf{v}_r = fluid velocity relative to the body

The drag and inertia coefficients are dictated by the model tests.

Drag

The BES TLP model has trapezium-shaped pontoons, but those can not be modelled with Orcaflex. To make the dynamic model as similar to the actual model as possible, the characteristics of the trapezium-shaped pontoon are mapped to a cylinder pontoon. The problem that comes in is that a cylinder can have either the correct volume or the correct projected area, but not both. Therefore, a correction of the drag coefficient (C_d) is applied to mimic the correct projected area. The cylinder diameter is determined by the volume calculated by ANSYS. The drag coefficient has to be adjusted by the ratio

between the area in ANSYS and the resulting projected area in Orcaflex. This can be done using the following relationship [78, 80]:

$$C_d^* = C_d \frac{A}{Dl} \quad (3.3)$$

where: D = diameter

l = length

C_d = user-defined drag coefficient

C_d^* = OrcaFlex drag coefficient

3.2.2.5. Mapping Structural Properties to Dynamic Model

Structural properties are calculated by Ansys (using the detailed structural model) and mapped to the different parts of the dynamic (with OrcaFlex) model and their connections.

These properties are section mass and mass gyration, section volume and surface area, section stiffness, and connection stiffness.

Section mass and mass gyration

For each element e , the shell element mass is:

$$m_e = (\rho At)_e \quad (3.4)$$

where: ρ = density of the material

A = surface area

t = thickness

And the total mass is:

$$m = \sum_{\forall e} m_e \quad (3.5)$$

Using centroid locations x , y , z , the mass moment of inertia (i.e. mass gyration) is defined by:

$$\begin{Bmatrix} I_x \\ I_y \\ I_z \end{Bmatrix} = \sum_{\forall e} m_e \begin{Bmatrix} x \\ y \\ z \end{Bmatrix}_e^2 \quad (3.6)$$

Section volume and surface area

The model's volume is important for OrcaFlex to compute right the buoyancy. Calculation of the volume of a mesh can be done by applying hydrostatic pressure to each element e :

$$p_e = h_e \rho g \quad (3.7)$$

The buoyancy becomes:

$$B = \sum_{\forall e} \vec{\mathbf{n}}_{z,e} \cdot p_e = V \rho g \quad (3.8)$$

where: $\vec{\mathbf{n}}_{z,e}$ = z-component of the element normal vector

h_e = depth of the point at which you're measuring the pressure, below the surface of the fluid

ρ = density of the fluid

g = gravity

From this follows that volume is independent of ρg .

$$V = \sum_{\forall e} \vec{\mathbf{n}}_{z,e} \cdot p_e \quad (3.9)$$

Let $\rho g = 1$, then the z-component of the reaction force is equal to the volume.

Section stiffness

The bending stiffness is computed as follows:

$$M = EI\kappa = EI \frac{d^2 w}{dx^2} \quad (3.10)$$

If we assume curvature κ is constant across the section length l , then:

$$\kappa = \frac{\phi}{l} \quad (3.11)$$

Let the forced rotation displacement be $\phi = 1 \text{ rad}$, the bending stiffness becomes:

$$EI = Ml \quad (3.12)$$

where: M = bending moment

EI = bending stiffness

The same principle applies to the axial stiffness.

Connection stiffness

It is calculated in the same manner as the section bending stiffness, but the resulting moment can be used directly.

3.2.3. Results

3.2.3.1. Response Analysis

For the optimal design of a monitoring system for a TLP that supports a FOWT, the structural behaviour of the platform is analyzed. This involves an exploration of how the structure responds to different environmental conditions, providing valuable insights into its dynamic characteristics.

The investigation entails dynamic simulations using the OrcaFlex software. These simulations examine the structure's response to different types of loads. The simulations are conducted under conditions such as hydrodynamic loads alone (including scenarios of waves only, and waves and current), wind alone, as well as a combination of wind and hydrodynamic loads. Then, the resulting stress on the structure

is analyzed. The assumption of the superposition of stresses is utilized, leading to an evaluation of the different stresses the structure may experience.

In the present work, the investigation involves a detailed analysis of the stress components experienced by the structure. Axial stress (denoted as σ_x , with x being the longitudinal axis), and bending stress (denoted as σ_z , with z being the vertical axis) are examined. Shear stress is also considered (denoted as σ_{xy} , where x specifies the orientation of the area to which the force is applied and y indicates the axis along which the shear stress acts). The maximum values of these stresses along the lengths of both a pontoon and the upper column of the TLP under various environmental conditions are summed up. Subsequently, the proportion each type of stress contributes to the total stress is evaluated. The table with all the percentages can be found in Appendix C, along with the characteristics of the different load cases (with different environmental conditions).

The contribution of axial stress to the total stress in the pontoons is relatively low, at a maximum of 3%. In the upper column, there is a more significant influence from axial stress, with its contribution ranging between 6% and 29%. The axial stress in the upper column is negative, indicating that it is compressive stress.

When environmental loading conditions incorporate wind, the bending response appears to predominantly influence both the upper column and the pontoons of the TLP. In the upper column, bending contributes to more than 88% of the total response (with the remainder being due to compression). In the pontoons, bending constitutes over 84% of the total response.

However, the involvement of hydro loads introduces a compression component in the response of the upper column. Under these circumstances, bending constitutes between 70% and 92% of the total response in the column (with the rest being compression mainly), and over 84% in the pontoons (with the rest being shear mainly). This compression results from the downward force of the turbine's weight (i.e. the tower and nacelle), counterbalanced by the upward force of the platform's buoyancy.

The bending in the pontoons comes from the vertical component of the tendon loads (acting downwards) combined with the buoyancy of the platform (acting upwards). Figure 3.10 shows the forces inducing the bending response in the pontoons.

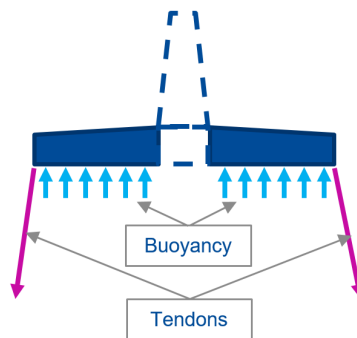


Figure 3.10: Response (bending) in pontoons.

The bending in the column results from the bending moment generated by the horizontal forces due to currents and waves (in the submerged part), and the wind (on the remaining part of the TLP and the tower). Considering that the turbine's tower has a height of 120m and there is a point mass at the top (the nacelle and rotor), the bending moment generated is significant and has a considerable influence on the column of the TLP. Figure 3.11 illustrates the forces generating the bending and the compression responses of the upper column of the TLP.

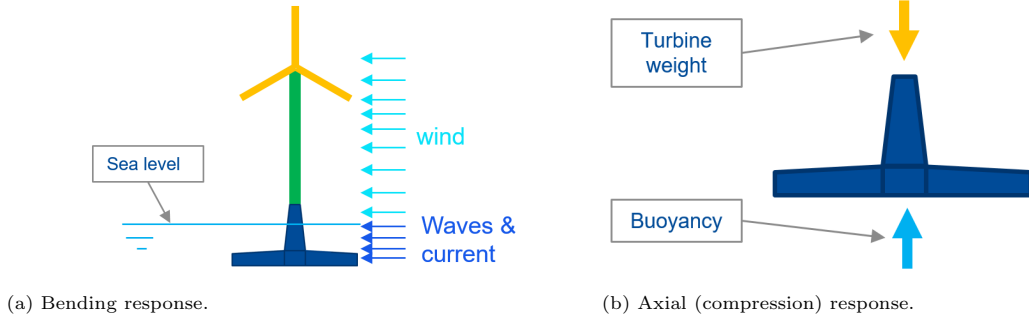


Figure 3.11: Response in pontoons.

The analysis reveals that the shear stress constitutes between 11% and 14% of the total stress experienced by the pontoons. In the upper column, it accounts for a maximum of 2% only. When compared to other stress components, the contribution of shear stress is relatively minor. Given this low contribution, it may be practical to dismiss the shear stress in further analysis.

This analysis concludes with the assumption that in all parts of the TLP, the governing stress is due to strain in the longitudinal direction. In the pontoons, this strain is due to bending deformation, and in the column as a consequence of axial and bending responses.

3.2.3.2. Modal Matrix

The modal matrix is derived from the modal analysis performed by Orcaflex. This analysis is based on the mathematical principles detailed in subsection 2.1.1. Orcaflex presents the mode shapes in terms of normalized translational and rotational offsets for each node.[81]

From the response analysis, the type of stresses to consider for each part of the TLP are selected. These stresses are proportionally related to the strains through Hooke's law (Equation 2.16). The strains have the same source (i.e. axial and bending responses). Strains are used in this analysis because the measurements of the monitoring system are strains. The strain due to axial stress is constant along the cross-section, and it is defined by:

$$\epsilon_{axial} = \frac{\delta}{L} \quad (3.13)$$

where δ is the change in length and L is the original length.

The strain due to bending is maximum in the outer fibers and 0 in the neutral axis, and it is described

by the following equation:

$$\varepsilon_{bending} = -\kappa y = \frac{M}{EI} y \quad (3.14)$$

where y is the distance from the neutral axis and the curvature κ depends on the bending stiffness EI and the bending moment M :

$$M = -EI \frac{\partial \theta}{\partial x} \quad (3.15)$$

where θ is the rotation.

The modal matrix in terms of strain is constructed with the axial and bending strains. The axial strain of each mode in the upper column is derived from the nodal vertical displacements (in the z direction) of each node using the following expression for the i_{th} element:

$$\varepsilon_i = \frac{\delta}{L_{initial}} = \frac{L_{final} - L_{initial}}{L_{initial}} = \frac{position_z[i+1] - position_z[i] - L_{element}}{L_{element}} \quad (3.16)$$

The maximum bending strain of each mode in the upper column for the i_{th} element is derived from the nodal vertical rotations (in the z direction) as follows:

$$\varepsilon_i = y_{max} \frac{\partial \theta}{\partial x} = y_{max} \frac{rotation_z[i+1] - rotation_z[i]}{L_{element}} \quad (3.17)$$

3.2.3.3. Numerical Response

The numerical response has two functions. It acts as the source from which measurements for response reconstruction are extracted. It also provides a point of reference for comparison with the reconstructed response, allowing for an assessment of the prediction's accuracy.

The response of a time stamp is taken from a numerical dynamic simulation (using Orcaflex). The environmental conditions selected for the simulation are a combination of all types of sources (i.e. wind, current, and waves) with a moderate intensity. The parameters of the environmental conditions such as wind speed (V_w), significant wave height (H_s), current speed (V_c), and the directions are shown in [Table 3.1](#).

	Wind	Waves	Current
Magnitude	$V_w = 20$ m/s	$H_s = 2$ m	$V_c = 1$ m/s
Direction	180°	180°	90°

Table 3.1: Sea state details.

Choosing a time stamp reflects a specific instant during the dynamic response of the FOWT, akin to the moment a strain gauge records a strain measurement. The dynamic simulation has a duration of 15 minutes. The first minute of the simulation was disregarded as it represents the initial transient phase when the structure starts to move. It results in higher levels of stress due to the abrupt introduction of forces on the structure. As the simulation continues, the structural response tends to converge to a more representative steady-state condition. Within this latter condition, the maximum response of the governing response (i.e. bending) is higher in the critical location (i.e. pontoon-column connection) is

second 382. This is the selected time stamp to investigate the response. This is represented in the time history results of the bending strain in the connection between a pontoon and the column of the TLP:

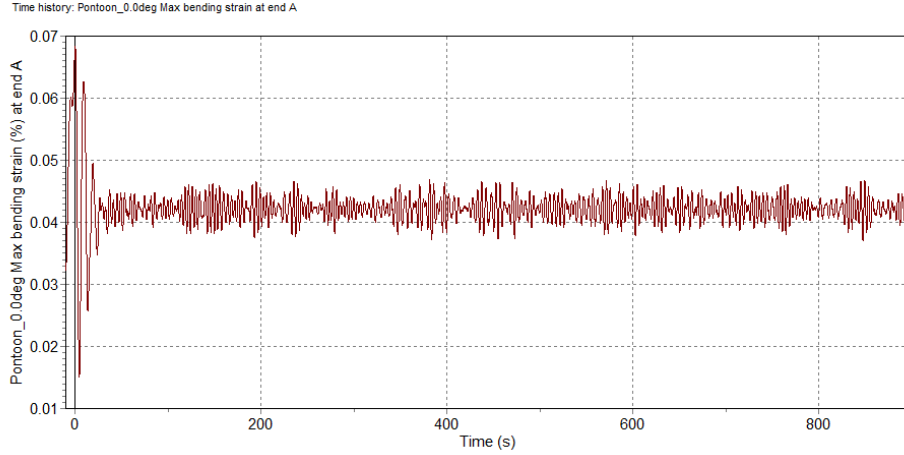
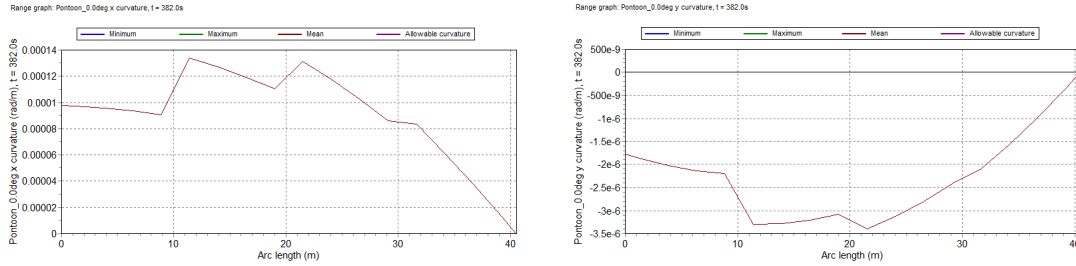


Figure 3.12: Time history of bending strain in pontoon-column connection.

Based on the superposition assumption, the total strain considered in the upper column is the sum of the considered types of strain (see Equation 3.18), this is the axial and bending strain. Orcaflex calculates the axial strain with Equation 3.13. The bending strain is computed with the same expression but in the outer fibers due to bending response. Then, the strain has the same direction but a different origin.

$$\varepsilon_{zz} = \varepsilon_{zz,axial} + \varepsilon_{zz,bending} \quad (3.18)$$

Specifically, the bending strain option selected in Orcaflex is *maximum bending strain*. This is because the governing bending direction is vertical. The curvature in the transverse direction is approximately 2% of the curvature in the vertical direction. Figure 3.13 shows the curvature (κ) in the vertical and transverse directions for the same time stamp ($t = 382$ s). The results obtained and used from Orcaflex are for each element.



(a) In the vertical direction.

(b) In the transverse direction.

Figure 3.13: Curvature in the pontoon aligned with the global X axis.

The numerical strain response for the time stamp $t = 382$ s and the sea state described in Table 3.1 in the pontoons of the TLP is shown in Figure 3.14. The pontoon aligned with the global X axis is named *pontoon 1*, the pontoon at 120° of that axis is *pontoon 2*, and the pontoon at 240° is *pontoon 3*. The strain values for the first and last points are extrapolated. The first point of the pontoons, (at $x = 0$ m) is extrapolated linearly based on the trend of the first two points, while the last point (at x

= 40.5 m) is extrapolated using a cubic function that fits the overall trend of the data. For the upper column, both points are extrapolated using a linear function that fits the overall trend of the data.

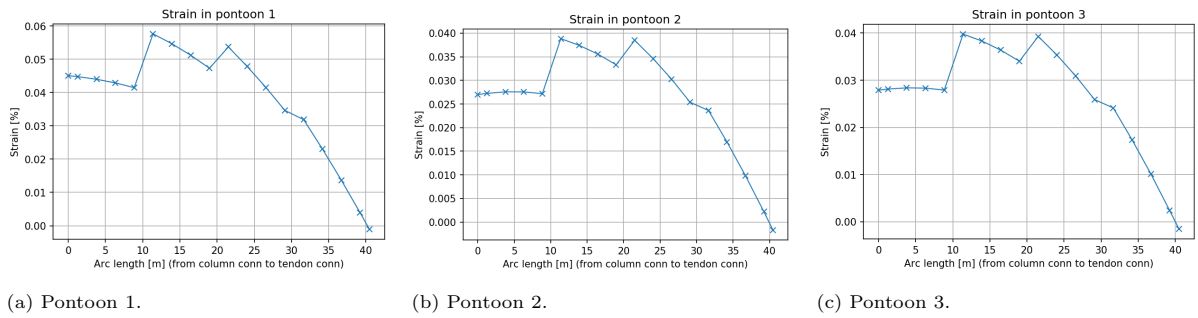


Figure 3.14: Strain response in the pontoons of the TLP.

The numerical response for the time stamp $t = 382$ s and the sea state described in Table 3.1 in the upper column of the TLP is shown in Figure 3.15:

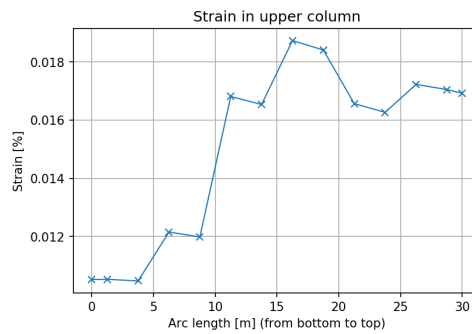


Figure 3.15: Strain response in the upper column of the TLP.

3.2.3.4. Selected Sea States

Different sea states serve diverse purposes for the design of a fatigue monitoring system.

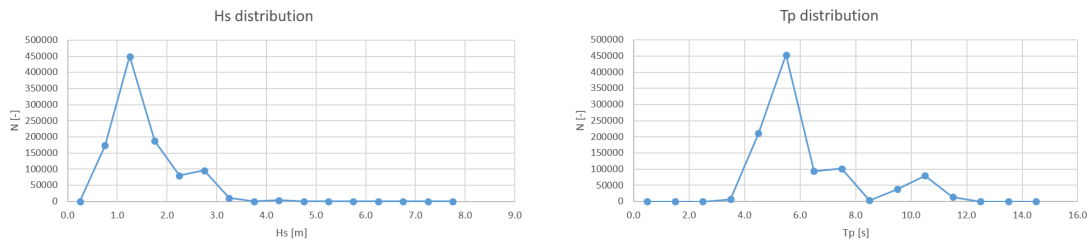
Fatigue-Contributing Sea States

For the fatigue assessment, the sea states contributing more to the platform fatigue are valuable. To select these sea states, a scatter diagram is generated using 100 sea states chosen by Bluewater (see Figure 3.16).

Hs [m]			TOTAL															
Min	Mean	Max	0	0	0	6421	210736	453302	93884	101352	3030	38140	79513	14017	0	0	0	1000395
7.50	7.75	8.00	0	0	0	0	0	0	0	0	0	0	0	0	0	0	0	0
7.00	7.25	7.50	0	0	0	0	0	0	0	0	0	0	0	0	0	0	0	0
6.50	6.75	7.00	0	0	0	0	0	0	0	0	0	0	0	0	0	0	0	0
6.00	6.25	6.50	0	0	0	0	0	0	0	0	0	0	0	0	0	0	0	0
5.50	5.75	6.00	0	0	0	0	0	0	0	0	0	0	0	0	0	0	0	0
5.00	5.25	5.50	0	0	0	0	0	0	0	0	0	0	0	117	0	0	0	117
4.50	4.75	5.00	0	0	0	0	0	0	0	0	0	0	0	0	0	0	0	0
4.00	4.25	4.50	0	0	0	0	0	0	0	0	0	3390	0	0	0	0	0	3390
3.50	3.75	4.00	0	0	0	0	0	0	0	0	0	0	0	0	0	0	0	0
3.00	3.25	3.50	0	0	0	0	0	701	816	0	0	3619	5840	0	0	0	0	10976
2.50	2.75	3.00	0	0	0	0	1520	37032	6536	1630	6650	39330	3390	0	0	0	0	96088
2.00	2.25	2.50	0	0	0	0	11737	38200	0	0	0	25614	4670	0	0	0	0	80221
1.50	1.75	2.00	0	0	0	0	117	130817	1051	16100	0	28100	10950	0	0	0	0	187135
1.00	1.25	1.50	0	0	0	467	62510	307128	0	77900	1400	0	0	0	0	0	0	449405
0.50	0.75	1.00	0	0	0	5954	148109	2100	16900	0	0	0	0	0	0	0	0	173063
0.00	0.25	0.50	0	0	0	0	0	0	0	0	0	0	0	0	0	0	0	0
Tp [s]	Min:	0.00	1.00	2.00	3.00	4.00	5.00	6.00	7.00	8.00	9.00	10.00	11.00	12.00	13.00	14.00		
	Mean:	0.50	1.50	2.50	3.50	4.50	5.50	6.50	7.50	8.50	9.50	10.50	11.50	12.50	13.50	14.50		
	max:	1.00	2.00	3.00	4.00	5.00	6.00	7.00	8.00	9.00	10.00	11.00	12.00	13.00	14.00	15.00	TOTAL	

Figure 3.16: Scatter diagram with 100 sea states.

It can be observed that the mean values of the significant wave height (H_s) and wave period (T_p) that can be more critical for the structure's fatigue are 2.35 m and 5.5 s respectively. This fact can also be observed Figure 3.17, illustrating the number of cycles (N) that each H_s and T (separately) can induce.

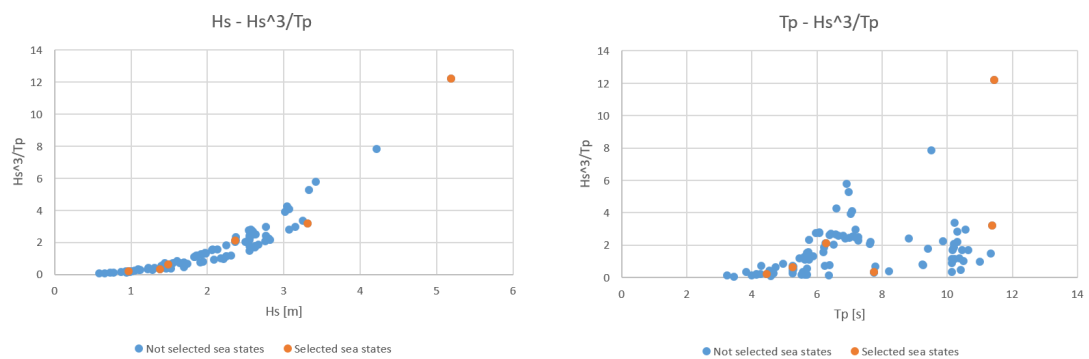


(a) Significant wave height distribution.

(b) Wave period distribution.

Figure 3.17: Number of cycles that each H_s and T_p can induce.

Figure 3.18 show an approximation of the wave power density (H_s^3/T_p) depending on the H_s and T_p . Figure 3.19 present the approximation of the wave power density considering as well the probability of occurrence (Occ). These plots allow another way of visualizing the impact of each significant wave height and wave period values to the fatigue lifetime of the structure.



(a) Wave power density depending on H_s .

(b) Wave power density depending on T_p .

Figure 3.18: Approximation of wave power density depending on significant wave height and wave period.

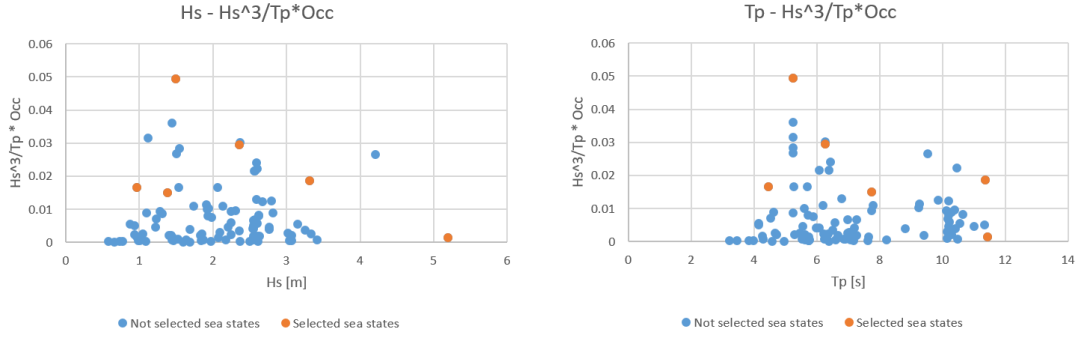
(a) Wave power density depending on H_s .(b) Wave power density depending on T_p .

Figure 3.19: Approximation of wave power density depending on significant wave height and wave period considering the probability of occurrence.

Based on this information, the chosen sea states are those considered the most contributing ones for the TLP fatigue. The orange points represent the selected sea states. Table 3.2 presents the characteristics of the waves (significant wave height H_s , wave period T_p , the peak enhancement factor γ and direction Wav_{dir}), wind (wind speed V_w and direction Win_{dir}) and current (current speed V_c and direction C_{dir}) along with the probability of occurrence.

Sea State ID	H_s [m]	T_p [s]	γ [-]	Wav_{dir} [°]	V_w [m/s]	Win_{dir} [°]	V_c [m/s]	C_{dir} [°]	Probability [-]
6	0.97	4.46	1.71	60	12	60	0.25	0	8.13E-02
19	1.38	7.75	1	240	12	300	0.25	240	4.38E-02
45	2.36	6.27	2.87	300	20	300	0.25	0	1.41E-02
48	1.49	5.25	2.25	300	12	300	0.25	2.4	7.83E-02
96	3.31	11.37	1	300	20	300	0.25	0	5.84E-03
100	5.19	11.44	1	240	20	300	0.75	300	1.17E-04

Table 3.2: Characteristics of the selected fatigue-contributing sea states.

Diverse Condition Sea States

Another set of sea states is selected to validate the versatility and robustness of the monitoring system. These include different environmental conditions with hydro loads only, wind only and a combination of both. These environmental sources are considered for mild, harsh and extreme conditions. The main objective of this selection is to evaluate whether the fatigue monitoring system can provide accurate predictions even with unexpected loading conditions. The characteristics of the sea states are presented in Table 3.3.

Sea State ID	H_s [m]	Wav_{dir} [°]	V_w [m/s]	$Wind_{dir}$ [°]	V_c [m/s]	C_{dir} [°]
101	2	180	20	180	1	90
102	2	180	-	-	1	90
103	-	-	20	180	-	-
104	5	180	30	180	3	90
105	5	180	-	-	3	90
106	-	-	30	180	-	-
107	10	180	40	180	6	90

Table 3.3: Characteristics of the selected sea states with diverse environmental conditions.

3.2.3.5. Response Reconstruction in TLP

Full-Field Strain Estimation

The full-field response estimation is useful for the verification of the design. With the continuous monitoring of the structural response in the entire TLP, the operators and designers can examine if the platform behaves as intended in the design.

The accuracy of the reconstruction for each TLP component (i.e. pontoons and upper column) is assessed using the mean percentage error corresponding to each respective part.

$$err = average \left(\frac{|\varepsilon_{numerical} - \varepsilon_{estimated}|}{\varepsilon_{numerical,max}} \cdot 100 \right) \quad (3.19)$$

Using the sea state number 101 described in Table 3.1, the full-field strain estimation is performed. For the reconstruction of the pontoons' responses, 3 sensors and 3 modes are used. The same amount of sensors as modes is utilized to avoid the problem being undetermined (if there are less amount of sensors than modes) and to use the measurement data from the exact desired location (sensor placement is key). The sensor placement and the governing modes selections are obtained using the algorithm described in chapter 4. The first sensor is placed at a distance of 1.27 m from the connection of the pontoon with the column, the second one at a distance of 13.92 m, and the last one at 31.64 m. The selected modes are the sway mode of the FOWT (i.e. mode 1), the surge mode (i.e. mode 2), and the heave mode (i.e. mode 6). Figure 3.20 shows the full-field strain estimation for each pontoon.

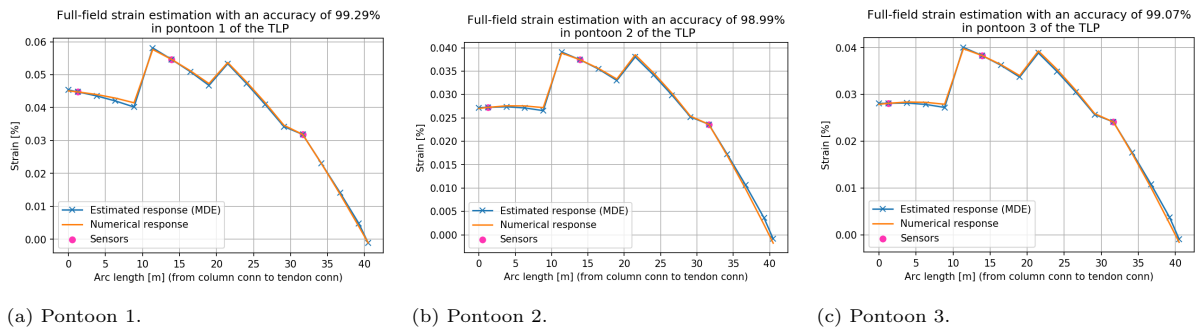


Figure 3.20: Full-field strain reconstruction for the pontoons of the TLP.

The reconstructions have an accuracy of over almost 99%.

Figure 3.21 allows to visualize the normalized numerical response along with the normalized strain mode shapes of the governing modes.

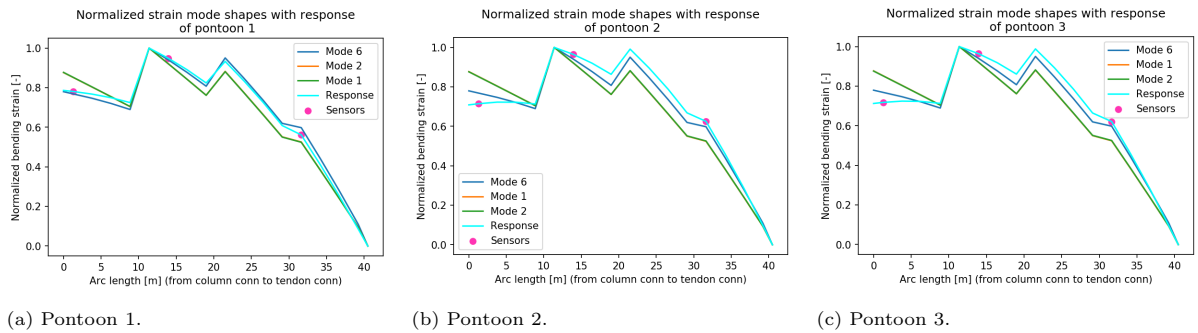


Figure 3.21: Numerical response along with the governing mode shapes for the pontoons of the TLP.

For the full-field strain estimation in the upper column of the TLP, 2 sensors and 2 modes are used. One sensor is located 6.25 m away from the lower column (i.e. at the bottom) and the other one is 26.25 m away. The considered modes for the reconstruction are the roll and pitch modes (modes 10 and 11, respectively), which are the bending modes of the column of the TLP and the turbine tower. This selection is explained in chapter 4. Figure 3.22 presents the full-field strain estimation for the upper column of the TLP.

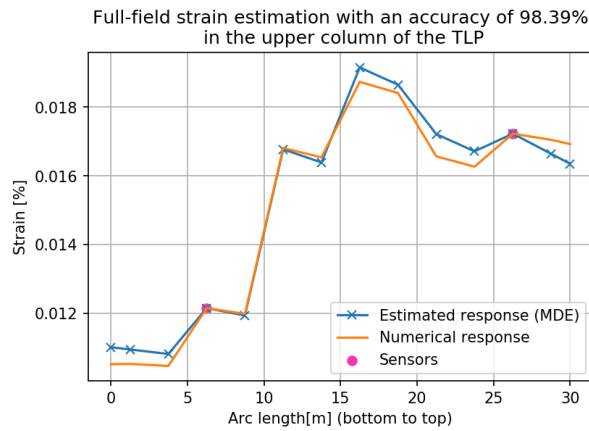


Figure 3.22: Full-field strain reconstruction for the upper column of the TLP.

The full-field strain estimation in the upper column of the TLP has an accuracy of 98.39%.

Figure 3.23 represents the normalized numerical response together with the governing normalized strain mode shapes.

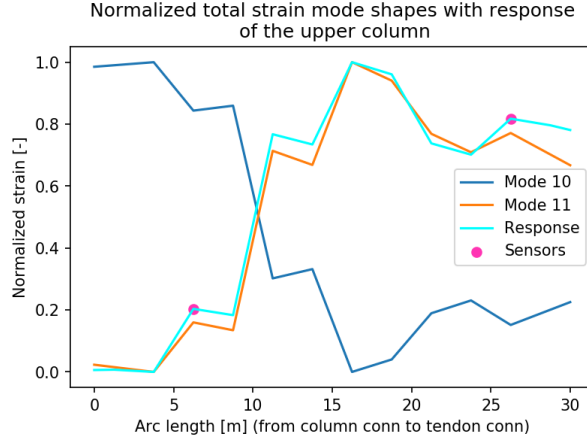


Figure 3.23: Numerical response along with the governing mode shapes for the upper column of the TLP.

Stress History Estimation in Critical Location

The fatigue assessment of the critical locations is helpful when estimating the remaining lifetime of the structure. The locations which are more prone to fatigue in the BES TLP are the pontoon-column connections and the change in diameter of the upper column. In this study, only the former is investigated. This is because the latter is due to a change in geometry which is not present in the model used.

The numerical stress in the critical location is computed using the numerical strain results. This is because Orcaflex uses an excessive moment of inertia I as a result of modifying the geometry to achieve the pursued structural properties. The strain computation uses the mapped stiffness properties (both bending and axial stiffness EI and EA , respectively) obtained using Ansys with the detailed BES TLP model. To convert the strain results in stress, Hooke's law (Equation 2.16) is used. The design of this model carried out by Bluewater determines that the Young's Modulus E of the material (i.e. steel) is 210 GPa. The point of the model representing the connection of the pontoon with the column is point 0 of the pontoon.

To evaluate the accuracy of the stress history estimation and its impact on the fatigue assessment, the Palmgren-Miner rule (Equation 3.20 recalled from Equation A.1) is used.

$$D = \sum_{i=1}^k \frac{n_i}{N_i} = \frac{1}{\bar{a}} \sum_{i=1}^k n_i \cdot (\Delta\sigma)^m \quad (3.20)$$

where: D = accumulated fatigue damage

\bar{a} = intercept of the design S-N curve with the log N axis

m = negative inverse slope of the S-N curve

k = number of stress blocks

$\Delta\sigma_i$ = stress range block

n_i = number of stress cycles in stress block i

N_i = number of cycles to failure at constant stress range $\Delta\sigma_i$

The accuracy of the standard deviation of the stress estimation is investigated to determine how the error propagates through the estimated accumulated fatigue damage and lifetime predictions. This is

achieved by raising the estimation error in the standard deviation (s_σ) by the slope of the S-N curve. In the case of the TLP, the "E" and "F" S-N curves from DNV-RP-C203: "Fatigue design of offshore steel structures" [84]. Both curves have two slopes: 3 and 5. For this assessment, the slope $m = 3$ is used, as it is assumed that the major part of the lifetime of the structure will occur within this slope. Lastly, multiplying the term by the probability of occurrence allows to understand the impact on the fatigue lifetime. Therefore, the error in the fatigue damage accumulation (D_{error}) is computed as follows:

$$D_{error} = s_\sigma^3 \cdot Occ \quad (3.21)$$

Figure 3.24 represents the stress history estimation for the most probable fatigue sea state (i.e. number 6). It has to be noted that the estimated signal is not clearly visible due to the fact that the estimated and the numerical signals are significantly similar. This is why the lines are overlapped.

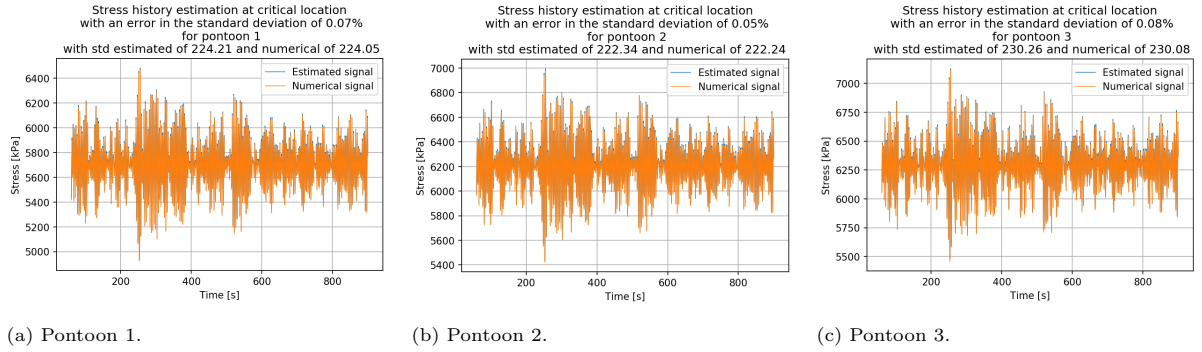


Figure 3.24: Stress histories of the 3 critical locations (i.e. pontoon-column connections).

In this case, 2 sensors placed 1.26 m and 8.86 m away from the critical location are used. The heave and the surge mode shapes conform the modal matrix. The selection of the sensor placements and governing modes is explained in chapter 4.

Using Equation 3.21, the error in the fatigue damage accumulation estimation for this sea state is 0.0024%.

3.2.4. Conclusions

The FOWT model was useful to obtain the global modes of the entire turbine and to perform dynamic simulations with diverse environmental conditions. The response analysis enabled to have knowledge about the structural response of the TLP. The bending response is governing in the pontoons, generating the major part of the stress. Bending and compression govern the response in the upper column. By having complete global modal matrices in terms of strain due to bending for the pontoons and due to both bending and compression in the upper column, the modes governing the response can be selected from this complete modal matrix.

The reconstruction of the structural response of the TLP using a limited amount of sensors could be performed accurately in a general sea state combining hydro and wind loads. Accuracies of over 98.39% could be achieved for the full-field strain estimations and 99.998% in the fatigue damage accumulation prediction. This section concludes that MDE can be applied for the structural response reconstruction of a TLP supporting a FOWT.

4

Design of Fatigue Monitoring System

4.1. Modal Selection

The mode shapes constituting the modal matrix used in the modal expansion (Equation 2.12) have to be carefully selected. This is useful to obtain an accurate reconstruction of the structural response.

4.1.1. Strain Energy

At first, the modal selection based on the strain energy (E) used by Bogert et al. [85] was considered. This approach explores the percentage of the strain energy of a mode (Equation 4.1) within the strain energy of the structural response (Equation 4.2). However, this approach requires the measurements to be displacements.

$$E_{modal} = \frac{1}{2} \mathbf{u}_{modal}^T \mathbf{K} \mathbf{u}_{modal} \quad (4.1)$$

$$E_{response} = \frac{1}{2} \mathbf{u}_{response}^T \mathbf{K} \mathbf{u}_{response} \quad (4.2)$$

where \mathbf{u}_{modal} and $\mathbf{u}_{response}$ are the displacement vectors of the mode and the response, and \mathbf{K} is the stiffness matrix of the structure. In this study, strain measurements are used.

Another definition of strain measurement is found:

$$E = \frac{1}{2} V \sigma \epsilon \quad (4.3)$$

The problem here is the assumption of the strain being uniformly distributed. This is not true for the case of the TLP.

In conclusion, strain energy can not be used for the modal selection in the present study.

4.1.2. Similarity

The degree of similarity between a mode shape and the structure's dynamic response is indicative of its representativeness and governing influence in the response. Cross-correlation between each strain mode shape and the strain response is used to assess the governance of the mode in the response. Each mode shape and the response are normalized from 0 to 1 to compare the shapes of the functions. This method focuses on the mode shape, not the magnitude.

The selection of the governing modes of the pontoons is initially conducted for one pontoon. Once the selection is completed, the results are applied to the other pontoons, as they have the same characteristics and are equally positioned around the column.

4.2. Sensor Layout Selection

4.2.1. Sensor Placement General Guidance

Sensors can not be located in hot spots because of high-stress gradients (which would make the measurement not accurate). They can also not be placed in boundaries as it would compromise their integrity.

The strain gauges assumed for this monitoring system are uni-axial (i.e. they measure strain in one direction). As a result of the response analysis, the governing stress in the TLP is due to strain in the longitudinal direction. This is why the strain gauges are planned to be located in the longitudinal directions for the pontoons and the column of the TLP.

In the column of the TLP, two sensor layouts are strategically placed to detect bending in the two principal directions, X and Y . In situations where the bending direction is not strictly along the X or Y axis, information from both sensor layouts is utilized. This approach is also applied to the pontoons. There are two sensor layouts: one to detect vertical bending and one for transverse bending.

In both the pontoons and the column, the placement of the sensors (whether on the upper or lower plates of the pontoons, or any face of the column) does not impact the identification of the bending strain. This is because bending strain generates one side of a component to be in compression (negative strain) and the opposite side to be in tension (positive strain).

The sensors should capture the global behaviour of the structure, given that MDE primarily considers global modes rather than local modes. To achieve this, it is advisable to position sensors where there is minimum interference of local effects (such as hydrodynamic and hydrostatic pressures). There are TLP components that are in contact with the sea and can experience the local hydro pressures. A solution to it can be to place the sensors on the sections of the plate situated directly above the bulkheads (as they avoid bending in plates).

4.2.2. Optimization Algorithm for Longitudinal Placement

The longitudinal position of the sensors is key in both the upper column and the pontoons.

4.2.2.1. Parameters

For this purpose, the placement is assessed based on specific parameters. These parameters are:

- **Differentiation of modes:** the distance between the normalized mode shapes at the sensor locations plays a significant role in MDE. If this distance is significant, it facilitates the identification and differentiation of the governing mode shape, enabling accurate reconstruction of the response from it.
- **Mode shape similarity:** the distance between the response and a mode shape indicates how governing a mode shape is in the response. If this distance is short (i.e. high similarity), it suggests that the specific mode shape significantly contributes to the response.
- **Modal amplitude:** the amplitude of the mode in the sensor placement is important as well for MDE. A higher modal amplitude in the sensor's position signifies a more detectable vibration, resulting in better detection of the governing modes.

An algorithm to select the best longitudinal placement for the sensors based on these parameters is developed.

4.2.2.2. Algorithm

The main steps that the algorithm follows are illustrated in [Figure 4.1](#) and described afterwards:



Figure 4.1: Main steps of the algorithm.

1. **Simulations:** It involves running a set of 10 minutes numerical simulations that generates a dataset. The simulations are run using all the considered sea states and all possible combinations of sensor layouts. The dataset is composed of a sensor layout with its associated prediction error (i.e. mean relative error along the TLP component) and parameters values. The parameters are defined as follows. The differentiation of modes for each point is the mean value of a set of distances between each normalized mode shape. The mode shape similarity is the distance between the normalized response to the closest normalized mode shape. The modal amplitude is the mean value of the amplitudes of the normalized mode shapes.
2. **Importances:** This step determines the influence of each parameter in minimizing the prediction error. This is obtained by generating a machine learning model using the Random Forest Regressor algorithm. The model is trained with the dataset generated from the dynamic simulations. The prediction error is the target variable and the predictors and the three parameters. Once the model is trained, the coefficient of contribution of each predictor is obtained with the "feature_importances_" attribute from the model.

3. **Scores:** The algorithm creates a score evaluation method for each set of possible sensor placements using a linear combination of the (scaled) features, each weighted by their coefficient of contribution (see Equation 4.4). The inverse value of *sim* represents the inverse relationship between the parameter and the error, as the smallest value of it generates a higher score to minimize the error.

$$score = diff \cdot C_{diff} + \frac{1}{sim} \cdot C_{sim} + ampl \cdot C_{ampl} \quad (4.4)$$

where: *diff* = scaled mean distance between the mode shapes
C_{diff} = coefficient of contribution of *diff* in minimizing the error
sim = scaled distance between the response and the closest mode shape
C_{sim} = coefficient of contribution of *sim* in minimizing the error
ampl = scaled mean value of the amplitudes of the mode shapes
C_{sim} = coefficient of contribution of *ampl* in minimizing the error

4. **Selection:** The final step is the selection process. It chooses the sensor layout with the highest associated score generated in the previous step. A higher score corresponds to a lower prediction error, based on the machine learning model.

4.3. Updated Design

The considerations for the design of the fatigue monitoring system are applied to a sensitivity analysis (chapter 5). This analysis enables to design a system that is as optimal as possible and versatile for different situations. Thus, the considerations previously explained are updated with this sensitivity analysis.

4.3.1. Upper Column

4.3.1.1. Sensor Layout Selection

Considering the sensor placement general guidance, some aspects are clear. Sensors should not be placed in hot spots or in boundaries. The sensors are uni-axial strain gauges positioned in the vertical direction. Two sensor layouts are placed in the main direction (i.e. *X* and *Y*).

The TLP specified by Bluewater has a draft of 24 m. A margin of 3 m is considered in case there are waves (for the waves' splashes not to interfere with the measurements or compromise the physical integrity of the sensor). For the sensors to not measure local pressures due to the sea, the area where they should be located is the top part where there is no contact with the sea. This has a height of 14 m. Within this dry area, the algorithm presented in subsection 4.2.2.2 is applied for the longitudinal sensor placement. The resultant placements are 16.25 m and 21.25 m away from the connection with the lower column.

4.3.1.2. Modal Selection

The modes that are more representative and should be used for the strain modal matrix in the upper column are the pitch and the heave global modes of the FOWT. These represent the bending and compressive local modes of the column and tower for the considered sea states, which are the governing responses found in the response analysis (see [subsubsection 3.2.3.1](#)). [Figure 4.2](#)

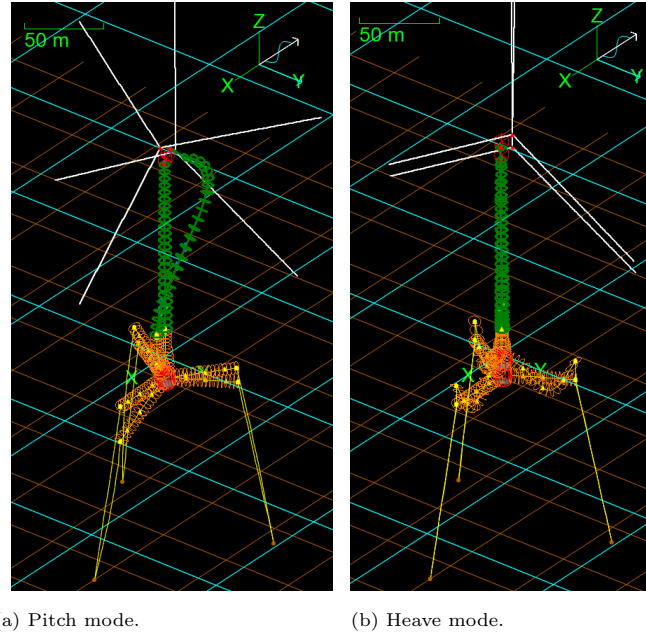


Figure 4.2: Governing modes in the dynamic response of the upper column of the TLP.

4.3.2. pontoons

4.3.2.1. Sensor Layout Selection

The same general considerations for the sensor placement for the upper column are followed for the pontoons.

As the pontoons are entirely submerged, a solution to minimize the interference of the local effects (such as hydrodynamic and hydrostatic pressures) is required. The sections of the plates of the pontoons which are placed above the bulkheads do not suffer significantly from these local effects. A suitable option is to place the sensors in those areas of the plates. In each pontoon, there are two transverse bulkheads. They are located at 16.89 m and 37.85 m away from the connection with the column.

4.3.2.2. Modal Selection

The most representative modes for the different sea states are heave and sway global modes. [Figure 4.3](#) illustrate them.

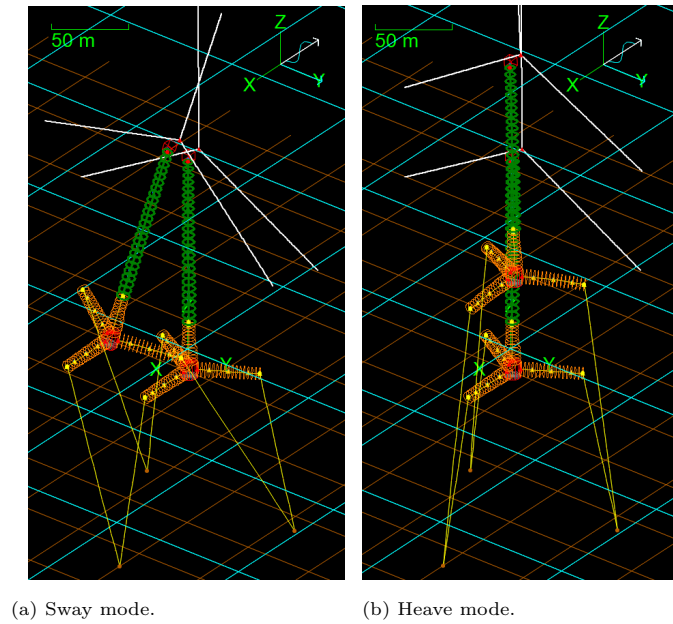
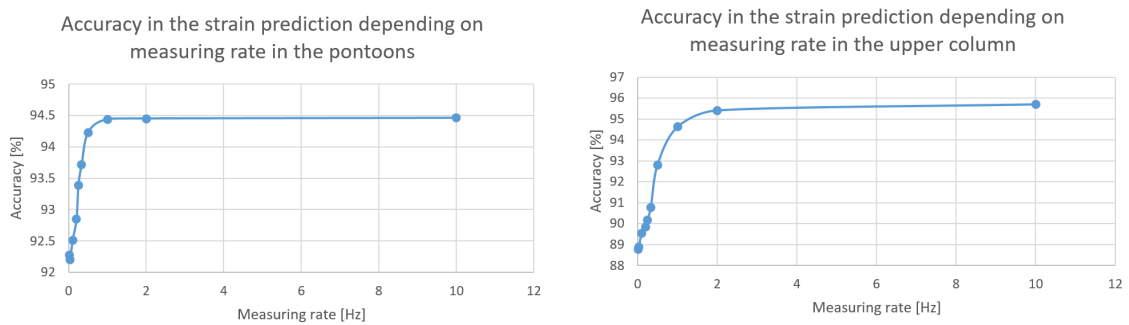


Figure 4.3: Governing modes in the dynamic response of the pontoons of the TLP.

4.3.3. Measuring Rate (or Sampling Rate)

The sensors have a certain measuring rate (also called sampling rate). To determine the measuring rate for this system, an investigation is performed. For it, the mean accuracy of the full-field strain estimations in the TLP components is analyzed with different sampling rates.



(a) In the pontoons.

(b) In the upper column.

Figure 4.4: Accuracy in the full-field strain estimations for each TLP component.

Observing the graphs, a common convergence takes place in both components from a measurement rate of 1 Hz, that is one sampling per second.

4.3.4. Model Validation

Model validation can be important for reliable and effective SHM. Ensuring that a monitoring system's predictions align closely with real-world observations ensure that any preventive or corrective measures taken are based on accurate data. This alignment between prediction and observation is particularly

crucial in marine structures, where consequences of overlooking details can be significant.

To achieve this validation, placing sensors at critical locations on the structure can be helpful. While computational models can predict stress and fatigue patterns, direct measurements from these vital zones offer empirical evidence. By observing stresses in these zones, one can directly compare predicted and actual stress behaviors, thereby providing a concrete basis for validation.

While the sensors might have their physical integrity compromised in those locations, the benefits of having real-time data from these essential areas far outweigh the associated challenges. In essence, the direct monitoring of critical zones bridges the gap between theoretical predictions and real-world observations, solidifying the reliability of the fatigue monitoring system.

4.3.5. Limitations

The present fatigue monitoring system primarily addresses the global behaviour of the structure. While this methodology provides valuable insights into the overall structural health, it may miss out on other stress sources.

Local responses coming from hydrostatic and hydrodynamic pressures, for instance, also contribute to the fatigue of the structure. The main limitation of this system is the fact that it does not consider these local responses.

4.3.6. Accuracy

The fatigue monitoring system presented in this study offers the following accuracy.

4.3.6.1. Full-Field Strain Estimation

For the pontoons, the mean relative error for each considered sea state are listed in [Table 4.1](#):

Sea state	6	19	45	48	96	100	101	102	103	104	105	106	107
Error [%]	94.5	94.65	95.07	96.23	94.9	95.78	94.4	94.61	93.68	94.65	94.73	93.73	90.75

Table 4.1: Mean error in the full-field strain estimation in the pontoons of the TLP per sea state.

And for the upper column, the mean errors of the response estimations are listed in [Table 4.2](#):

Sea state	6	19	45	48	96	100	101	102	103	104	105	106	107
Error [%]	88.88	90.14	97.87	98.43	98.29	98.48	96.92	91.65	97.23	92.35	90.78	96.08	92.91

Table 4.2: Mean error in the full-field strain estimation in the upper column of the TLP per sea state.

4.3.6.2. Stress History Estimation in Critical Location

The error in fatigue damage accumulation for all the fatigue-contributing sea states are shown in [Table 4.3](#):

Sea state	6	19	45	48	96	100
D_{error} [%]	0.006	0.006	0.0001	1.01E-05	0.0003	6.27E-05

Table 4.3: Error in fatigue damage accumulation for each fatigue-contributing sea state.

5

Sensitivity Analysis

5.1. Number of Modes and Sensors

5.1.1. Number of Sensors

For this sensitivity analysis, the sensor layouts and governing modes selections are performed using the algorithms described in [chapter 4](#). The sea state chosen for this analysis is the number 101 due to its general applicability.

The accuracy of the full-field strain estimation is assessed for both one pontoon and the upper column, using mean relative error expressed in percentage form and [Equation 5.1](#).

$$accuracy = 100 - error \quad (5.1)$$

For fatigue assessment, additional sensor layouts are explored to minimize the error in estimating the stress history in the critical location. Here, accuracy is evaluated using the mean relative error in the stress prediction across the entire simulation (i.e. 14 min), along with the relative error in the standard deviation estimation of the stress history.

This process is repeated for different numbers of sensors to evaluate the optimal number of sensors.

The different accuracy of the full-field strain estimations using various amounts of sensors in one pontoon and the upper column of the TLP are presented in [Figure 5.1](#).

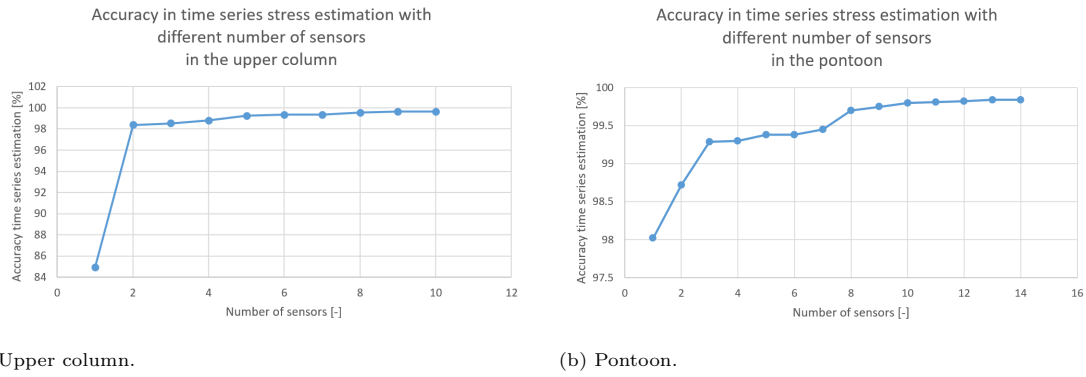


Figure 5.1: Sensitivity analysis on the number of sensors for full-field strain estimation.

Regarding the stress history estimation, the sensitivity analysis is presented in [Figure 5.2](#).

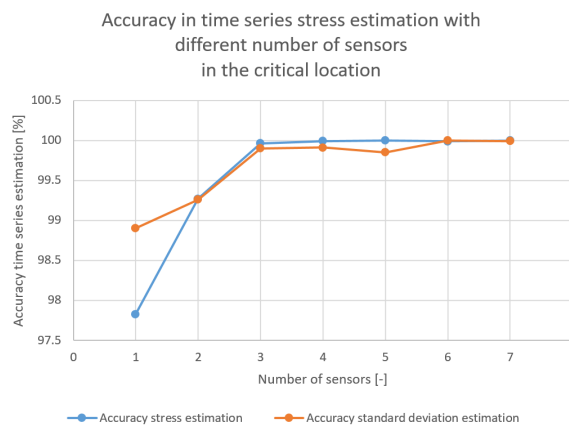


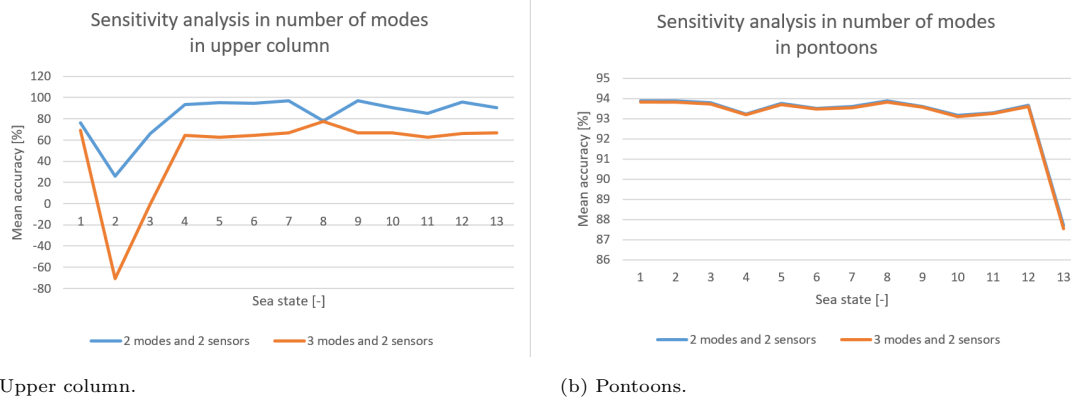
Figure 5.2: Sensitivity analysis on the number of sensors for stress history estimation in the critical location.

However, to capture the global behaviour of the structure, the sensors have to be placed in the areas of the plate on top of the bulkheads, as explained in [chapter 4](#). In each pontoon, there are 2 bulkheads. This is why the number of sensors in each sensor layout (for the different bending directions) in each pontoon should be 2.

5.1.2. Number of Modes

The number of modes considered for the modal matrix is limited by the number of sensors [53]. If there are more modes than sensors, interpolation becomes necessary to estimate the measurements of the same amount of modes (i.e. in other locations). Using MDE, the measurement locations are key for accurate predictions. Therefore, if the measured data is not from the initially desired measurement locations, it can result in less accurate predictions. This is observed in the beam analysis ([Appendix B](#)).

For the FOWT model, the analysis is performed to see how having more modes than sensors affects the prediction's accuracy. For it, the estimations are performed for the case of using the same amount of modes as sensors but also for more [Figure 5.3](#) illustrates the accuracies of the full-field strain estimation for each considered sea state.



(a) Upper column.

(b) pontoons.

Figure 5.3: Sensitivity analysis on the number of modes for full-field strain estimation.

In the case of this model, for the pontoons, there is no significant change in the prediction accuracy. However, for the upper column, there is.

5.1.3. Conclusions

There is a convergence in the accuracy for the upper column's response reconstruction using 2 sensors and for the pontoon, this convergence occurs from the use of 3 sensors. The optimal amount of sensors for the stress history estimation is found to be 3 for the sea state number 101.

The number of modes used should be the same as the number of sensors.

5.2. Unknown Loading Conditions

An SHM system should be able to provide accurate results regardless of the loading conditions. To determine if this is the case for the present monitoring system, a sensitivity analysis evaluating the accuracy of the response estimation is performed.

The general design considerations described in [chapter 4](#) are applied for all the sea states. These design considerations are updated to suit different loading conditions. This is achieved by analyzing and identifying the most frequently occurring optimal modes and sensor layouts for each sea state.

5.2.1. Modal Selection

The similarity approach has been applied to all sea conditions. The mode shapes presenting a higher correlation coefficient with the response for each condition are identified. The modes that frequently demonstrate higher similarity under various loading conditions are then recognized. Those are tested with the complete set of considered sea states.

The result of this sensitivity analysis is applied to the updated design.

5.2.2. Sensor Placement

A common longitudinal placement of the sensors is also selected on the basis of the best layouts for all the considered sea states using the algorithm and the general considerations.

5.2.3. Conclusions

Setting a common modal selection and sensor placement for all the considered sea states, the full-field strain estimation has a minimum accuracy of 88.9%, and the standard deviation estimation of the stress history in the critical location has a minimum accuracy of 90.8%. For the considered environmental conditions, there presented fatigue monitoring system performs the response estimation with acceptable accuracy.

5.3. Mass Distribution

Recalling [Equation 2.7](#), the mass matrix is part of the eigenvalue problem to obtain the mode shapes later used in the reconstruction of the response. There can be inaccuracies in the mass matrix due to errors in the model. This is why an evaluation of the sensitivity of the methodology when facing inaccurate mass distribution can be valuable.

There can be two possible modelling errors in the mass distribution: point masses and the added mass.

5.3.1. Point Masses

The point masses represent mass that is not part of the geometry (such as ladders or stairs in the tower). These masses of the FOWT model sum a total mass of 203.3 t, which represent the 8% of the total mass of the model (i.e. 2537.1 t).

There are two investigated cases. In the first one, the column's auxiliary masses and the tendon connectors are moved 5 m and the tower masses are moved 10 m. This change in the mass distribution generates an error in the response prediction lower than 0.02%. In the second case, all the masses are moved the same amount as in the previous case with the addition of increasing all these masses by a factor of 2. In this situation, the change in the response prediction's accuracy is 0.04%.

5.3.2. Added Mass

Added mass is the additional inertia required to move surrounding water as the structure moves. Using Newton's law ([Equation 5.2](#)), this extra force can be perceived as an additional mass that also needs to be accelerated.

$$F = m * a \tag{5.2}$$

The added mass associated with the pontoons is modified with increments and reductions of 20%. To understand the impact of this change on the total mass, [Equation 5.3](#) [81] is used. With it, the 20% of

the added mass of the pontoons (i.e. 1483.8 t) is found to be the 15.7% of the total displaced mass (i.e. 9445.1 t).

$$m_{added} = C_a \rho V \quad (5.3)$$

where ρ is the density of the fluid and V is the volume of the displaced fluid.

By modifying it, the standard deviation estimation of the stress history in the critical location is changed by a maximum of 0.2% when increasing or decreasing the added mass by 20%.

Irregular changes in the mass modelling are also investigated. The added mass in only one pontoon is increased and decreased by 20%. With this change, the centre of mass of the structure is moved 3.8 mm away from and toward the pontoon. The total width of the TLP is 92 m, so this movement is only 0.004%. The change in the standard deviation estimation accuracy of the stress history is 0.5%.

5.3.3. Conclusions

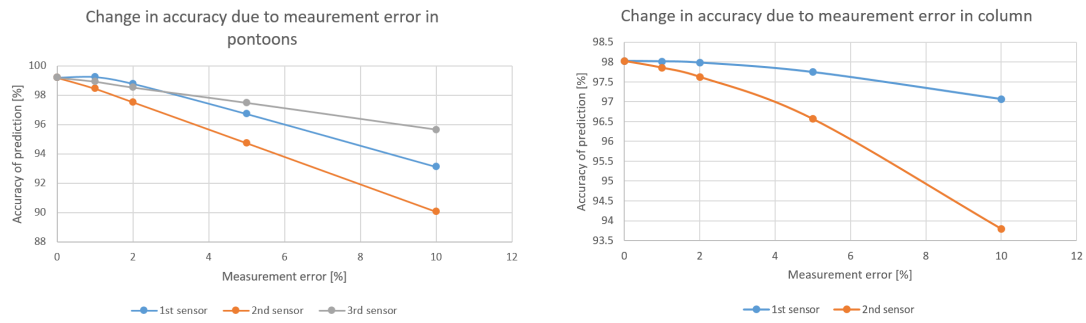
Errors in the mass modelling do not affect significantly the accuracy of the response estimations. To justify this conclusion, the impact of differences in the mass matrix in the mode shapes and natural frequencies is investigated.

To do it, the change in added mass of the pontoons of 20%. The mode shapes obtained with the modified mass matrix are normalized from 0 to 1 as well. The normalized mode shapes obtained with both the original and the modified mass matrix are compared using the correlation coefficient. This coefficient, when squared, is called the coefficient of determination or R-squared. If it is multiplied by 100, it represents the percentage of similarity between two functions (when it is subtracted from 100, it represents the percentage of variance). In the case of the governing modes, the percentage of variance of the mode shapes is not higher than 0.02%. The comparison of the natural frequencies with different mass matrices is performed with the percentage error. The difference in the calculated natural frequencies for the governing modes is approximately 5%.

As can be observed, the differences in the mass matrix have a higher impact on the natural frequency calculation. This justification is aligned with the fact that MDE does not use natural frequencies for the reconstruction of the structural response.

5.4. Measurement Error

In the real world is very possible that the sensors can have measurement errors. Because of this, the sensitivity of the system in front of measurement errors is investigated. Usually, strain gauges can have a measurement error of 1%, 2%, 5%, and up to 10% [86]. In [Figure 5.4](#), the change in accuracy of the structural response prediction depending on various measurement errors in the different sensors is illustrated.



(a) In the pontoons of the TLP.

(b) In the upper column of the TLP.

Figure 5.4: Accuracy of structural response prediction with different measurement errors.

5.4.1. Conclusions

Measurement errors can affect the accuracy of the response estimation. However, within the range of typical errors that strain gauges can have, the decrease in accuracy is not significant. The accuracy of the prediction remains over 90%.

6

Conclusions and Future Recommendations

6.1. Conclusions

In this research, the design of a fatigue monitoring system for a TLP supporting a FOWT is proposed. The main research question addressed is:

What are the required characteristics of a fatigue monitoring system using MDE for a TLP supporting a FOWT?

This question can be answered with the following sub-questions:

1. **Is the application of MDE suitable for reconstructing the structural response of a TLP supporting a FOWT?**

Modal Decomposition and Expansion (MDE) can provide accurate full-field strain estimations and fatigue damage accumulation predictions with a limited set of measurements. MDE can be suitable for structures that are subject to dynamic-driven loading conditions (like TLPs supporting FOWTs) because it can capture the dynamic behaviour of the structure. This methodology can be used for a fatigue monitoring system, allowing for the verification of the design considerations and the assessment of the remaining lifetime of the TLP.

2. **How sensitive is MDE for the fatigue monitoring of a simple structure (e.g. cantilever beam) to the measurement error, unexpected loading conditions, and different amounts of modes and sensors?**

If all sensors have a measurement error of up to 5% the change in accuracy is slightly notable in the hot spot strain prediction from the investigations performed on a cantilever beam. MDE can provide good response reconstruction for bending responses (when the directions of the bending are combined the predictions are still accurate). For torsion responses, the stress history in the critical location is precisely estimated, unlike the full-field strain estimation. When only axial

forces are applied, the reconstruction can become inaccurate. The number of modes and sensors is recommended to be the same. If there are more sensors than modes, the measurements are interpolated to undesired locations. Sensor location is key for accurate estimations.

3. What is the optimal sensor layout for the monitoring system?

Strain gauges capable of measuring low-frequency responses are considered to be suitable for a fatigue monitoring system for a TLP supporting a FOWT. Due to the response of the entire TLP being governed by normal stress/strain in the longitudinal direction, uniaxial strain gauges should be placed parallel to the longitudinal axis. Four sensors in the upper column and four sensors in each pontoon (i.e. sixteen sensors in total) can be a suitable sensor layout for the FOWT model used in Orcaflex. The sensors of the pontoons should be placed on the areas of the plate that remain just on top of the bulkheads. For the pontoons, the sensors should be placed in the dry area (i.e. not submerged) at 16.25 m and 21.25 m. The sampling rate should be 1 Hz. This system can provide full-field strain estimations of over 88.9% accuracy and fatigue damage accumulation predictions with errors of less than 0.01%.

4. How sensitive is the monitoring system to the mass distribution, measurement error, number of modes and sensors, or unknown loading conditions?

The methodology is insignificantly sensitive to differences in mass distribution, as they affect the calculation of the natural frequencies and not the mode shapes. MDE only uses the mode shapes to perform the response reconstruction. The number of modes is recommended to equal the number of sensors to obtain accurate predictions. The sensor layout and the modal selection can be adapted to the different considered sea states. Measurement errors can affect the prediction's accuracy, but not significantly.

6.2. Future Recommendations

Further research is recommended to understand and mitigate the impact of measurement noise in the fatigue monitoring system. This involves identifying the sources of noise and developing algorithms or using filtering techniques to minimize the noise. This management of noise can enhance the accuracy and reliability of the fatigue monitoring system.

This type of monitoring system can include accelerometers in the sensor layout [9, 45, 53, 63]. The incorporation of accelerometers (considering the response frequency range) can be investigated.

A limitation of the current designed system is the fact that it only monitors fatigue damage due to the global behaviour of the structure. Local pressures in the plates also contribute to the fatigue damage of the structure. A future recommendation is to add sensors to capture the stress due to these local pressures.

Incorporating a detailed FE model can enhance the accuracy of the analysis. The FE model allows for a deeper exploration of the stress and strain distribution, and potential fatigue locations. It also enables a more detailed geometry representation. As a result, the FE model can closely mimic the real

structure, leading to a more precise fatigue monitoring system.

The present study is performed by considering individually each TLP component. Another aspect to research further is establishing relationships between the sensors placed in the columns and in the pontoons of the TLP. This may lead to the omission of some sensors, resulting in a more efficient and optimized monitoring system.

Bibliography

- [1] S. Bhattacharya, *Design of Foundations for Offshore Wind Turbines*, 12 2018.
- [2] D. Arent, P. Sullivan, D. Heimiller, A. Lopez, K. Eurek, J. Badger, H. E. Jorgensen, M. Kelly, L. Clarke, and P. Luckow, “Improved offshore wind resource assessment in global climate stabilization scenarios,” 10 2012. [Online]. Available: <https://www.osti.gov/biblio/1055364>
- [3] A. Ciuriuc, J. I. Rapha, R. Guanche, and J. L. Domínguez-García, “Digital tools for floating offshore wind turbines (fowt): A state of the art,” *Energy Reports*, vol. 8, pp. 1207–1228, 2022. [Online]. Available: <https://www.sciencedirect.com/science/article/pii/S2352484721014736>
- [4] T. Wang, H. Jin, and X. Wu, “Coupled dynamic analysis of tlp floating offshore wind turbine,” *Journal of Offshore Mechanics and Arctic Engineering*, vol. 142, p. 1, 06 2019.
- [5] W. Leffler, R. Pattarozzi, G. Sterling, and R. Sorkhabi, “Deepwater petroleum exploration & production: A non-technical guide,” 01 2003.
- [6] S.-H. Ju, F.-C. Su, Y.-P. Ke, and M.-H. Xie, “Fatigue design of offshore wind turbine jacket-type structures using a parallel scheme,” *Renewable Energy*, vol. 136, pp. 69–78, 2019. [Online]. Available: <https://www.sciencedirect.com/science/article/pii/S0960148118315180>
- [7] P. H. Wirsching and Y.-N. Chen, “Considerations of probability-based fatigue design for marine structures,” *Marine Structures*, vol. 1, no. 1, pp. 23–45, 1988. [Online]. Available: <https://www.sciencedirect.com/science/article/pii/0951833988900093>
- [8] R. B. Hageman, “Uncertainty quantification of fatigue design loads when compared with in-service measurements on ship-shaped,” Ph.D. dissertation, 2022.
- [9] K. Maes, A. Iliopoulos, W. Weijtjens, C. Devriendt, and G. Lombaert, “Dynamic strain estimation for fatigue assessment of an offshore monopile wind turbine using filtering and modal expansion algorithms,” *Mechanical Systems and Signal Processing*, vol. 76-77, pp. 592–611, 2016. [Online]. Available: <https://www.sciencedirect.com/science/article/pii/S0888327016000066>
- [10] C. R. Farrar and K. Worden, “An introduction to structural health monitoring,” *Philosophical Transactions of the Royal Society A: Mathematical, Physical and Engineering Sciences*, vol. 365, no. 1851, pp. 303–315, 2007.
- [11] M. Celebi, “Seismic instrumentation of buildings (with emphasis on federal buildings),” Report No. 0-7460-68170, United States Geological Survey, Menlo Park, CA, Tech. Rep., 2002.
- [12] T. A. P. Lopes and N. F. Ebecken, “In-time fatigue monitoring using neural networks,” *Marine structures*, vol. 10, no. 5, pp. 363–387, 1997.
- [13] A. Ioannou, A. Angus, and F. Brennan, “A lifecycle techno-economic model of offshore wind energy for different entry and exit instances,” *Applied Energy*, vol. 221, pp. 406–424, 2018. [Online]. Available: <https://www.sciencedirect.com/science/article/pii/S0306261918304811>
- [14] A. Myhr, C. Bjerkseter, A. Ågotnes, and T. A. Nygaard, “Levelised cost of energy for offshore floating wind turbines in a life cycle perspective,” *Renewable Energy*, vol. 66, pp. 714–728, 2014. [Online]. Available: <https://www.sciencedirect.com/science/article/pii/S0960148114000469>
- [15] M. Shafiee, F. Brennan, and I. Espinosa, “A parametric whole life cost model for offshore wind farms,” *The International Journal of Life Cycle Assessment*, vol. 21, 07 2016.

- [16] H. Speckmann and R. Henrich, "Structural health monitoring (shm)," in *IMRBPB Meeting, EASA, Cologne*, vol. 12, 2007.
- [17] Y. Jiahui and M. Ren, "Tlp hull structural design and analysis." *Journal of Engineering Sciences and Technology*, vol. 84, pp. 35–40, 2013.
- [18] Apr 2023. [Online]. Available: <https://www.bluewater.com/>
- [19] E. Muehlner, "Tension leg platform (tlp)," *Encyclopedia of Maritime and Offshore Engineering*, pp. 1–10, 2017.
- [20] Y. Teng, J. Tan, J. Kim, H. Jang, and A. Baquet, "Tension leg platform design with consideration of tendon springing and ringing," in *Offshore Technology Conference Asia*. OnePetro, 2016.
- [21] A. Naess, "Prediction of extremes of combined first-order and slow-drift motions of offshore structures," *Applied Ocean Research*, vol. 11, no. 2, pp. 100–110, 1989. [Online]. Available: <https://www.sciencedirect.com/science/article/pii/0141118789900114>
- [22] Z. Du, X. Li, W. Xu, H. Zhu, J. Feng, W. Shen, and R. Jin, "An experimental investigation on vortex-induced motion (vim) of a tension leg platform in irregular waves combined with a uniform flow," *Applied Ocean Research*, vol. 123, p. 103185, 2022. [Online]. Available: <https://www.sciencedirect.com/science/article/pii/S0141118722001286>
- [23] J. H. C. Tan, Y. J. Teng, A. Magee, B. T. H. Ly, and S. Bhat Aramanadka, "Vortex induced motion of tlp with consideration of appurtenances," in *International Conference on Offshore Mechanics and Arctic Engineering*, vol. 45400. American Society of Mechanical Engineers, 2014, p. V002T08A025.
- [24] J. Kang, L. Sun, H. Sun, and C. Wu, "Risk assessment of floating offshore wind turbine based on correlation-fmea," *Ocean Engineering*, vol. 129, pp. 382–388, 2017. [Online]. Available: <https://www.sciencedirect.com/science/article/pii/S0029801816305558>
- [25] "DNV-ST-0119 Floating wind turbine structures," DET NORSKE VERITAS AS, Standard, Jun. 2021.
- [26] E. E. Bachynski, "Design and dynamic analysis of tension leg platform wind turbines," Ph.D. dissertation, 2014.
- [27] J. M. Jonkman, "Dynamics modeling and loads analysis of an offshore floating wind turbine," 12 2007. [Online]. Available: <https://www.osti.gov/biblio/921803>
- [28] L. Yu, S. Bhattacharya, L. Li, and Z. Guo, "Dynamic characteristics of offshore wind turbines on different types of foundations," *Electronic Journal of Geotechnical Engineering*, vol. 19, pp. 2917–2936, 01 2014.
- [29] J. López-Queija, E. Robles, J. Jugo, and S. Alonso-Quesada, "Review of control technologies for floating offshore wind turbines," *Renewable and Sustainable Energy Reviews*, vol. 167, p. 112787, 2022. [Online]. Available: <https://www.sciencedirect.com/science/article/pii/S1364032122006712>
- [30] B. R. Munson, D. F. Young, T. H. Okiishi, and W. W. Huebsch, "Fundamentals of fluid mechanics, john wiley & sons," *Inc., USA*, 2006.
- [31] F. A. Hashim, K. Hussain, E. H. Houssein, M. S. Mabrouk, and W. Al-Atabany, "Archimedes optimization algorithm: a new metaheuristic algorithm for solving optimization problems," *Applied Intelligence*, vol. 51, pp. 1531–1551, 2021.
- [32] K. F. Svendsen, "Structural design and dynamic analysis of a tension leg platform wind turbine, considering elasticity in the hull," Master's thesis, NTNU, 2016.
- [33] E. Rongé, C. Peyrard, M. Benoit, F. Robaux, and V. Venugopal, "A comparison of engineering third-order wave load models for bottom seated and truncated vertical cylinders," 11 2022.
- [34] M. Shen, Z. Hu, and G. Liu, "Dynamic response and viscous effect analysis of a tlp-type floating wind turbine using a coupled aero-hydro-mooring dynamic code," *Renewable Energy*, vol. 99, pp. 800–812, 2016. [Online]. Available: <https://www.sciencedirect.com/science/article/pii/S0960148116306735>
- [35] M. Klinikov and C. P. Fritzen, "An updated comparison of the force reconstruction methods," in *Key Engineering Materials*, vol. 347. Trans Tech Publ, 2007, pp. 461–466.

- [36] P. Guillaume, E. Parloo, and G. De Sitter, "Source identification from noisy response measurements using an iterative weighted pseudo-inverse approach," in *Finds and Results from the Swedish Cyprus Expedition: A Gender Perspective at the Medelhavsmuseet*, 2002.
- [37] E. Jacquelin, A. Bennani, and P. Hamelin, "Force reconstruction: analysis and regularization of a deconvolution problem," *Journal of sound and vibration*, vol. 265, no. 1, pp. 81–107, 2003.
- [38] Z. Lu and S. Law, "Force identification based on sensitivity in time domain," *Journal of Engineering Mechanics*, vol. 132, no. 10, pp. 1050–1056, 2006.
- [39] S. Eftekhari Azam, E. Chatzi, and C. Papadimitriou, "A dual kalman filter approach for state estimation via output-only acceleration measurements," *Mechanical Systems and Signal Processing*, vol. 60-61, pp. 866–886, 2015. [Online]. Available: <https://www.sciencedirect.com/science/article/pii/S0888327015000746>
- [40] J.-J. Liu, C.-K. Ma, I.-C. Kung, and D.-C. Lin, "Input force estimation of a cantilever plate by using a system identification technique," *Computer methods in applied mechanics and engineering*, vol. 190, no. 11-12, pp. 1309–1322, 2000.
- [41] C.-K. Ma, J.-M. Chang, and D.-C. Lin, "Input forces estimation of beam structures by an inverse method," *Journal of sound and vibration*, vol. 259, no. 2, pp. 387–407, 2003.
- [42] C.-K. Ma and C.-C. Ho, "An inverse method for the estimation of input forces acting on non-linear structural systems," *Journal of Sound and Vibration*, vol. 275, no. 3-5, pp. 953–971, 2004.
- [43] S. Xu, X. Deng, V. Tiwari, M. A. Sutton, W. L. Fourney, and D. Bretall, "An inverse approach for pressure load identification," *International Journal of Impact Engineering*, vol. 37, no. 7, pp. 865–877, 2010.
- [44] P. Aalberts, J. van der Cammen, and M. L. Kaminski, "Ss: Fpsos and floating production systems: The monitas system for the glas dowr fpso," in *Offshore Technology Conference*. OnePetro, 2010.
- [45] M. Tarpø, B. Nabuco, C. Georgakis, and R. Brincker, "Expansion of experimental mode shape from operational modal analysis and virtual sensing for fatigue analysis using the modal expansion method," *International Journal of Fatigue*, vol. 130, p. 105280, 2020. [Online]. Available: <https://www.sciencedirect.com/science/article/pii/S0142112319303846>
- [46] J.-J. Liu, C.-K. Ma, I.-C. Kung, and D.-C. Lin, "Input force estimation of a cantilever plate by using a system identification technique," *Computer Methods in Applied Mechanics and Engineering*, vol. 190, no. 11, pp. 1309–1322, 2000. [Online]. Available: <https://www.sciencedirect.com/science/article/pii/S004578259900465X>
- [47] C. Papadimitriou, C.-P. Fritzen, P. Kraemer, and E. Ntotsios, "Fatigue predictions in entire body of metallic structures from a limited number of vibration sensors using kalman filtering," *Structural Control and Health Monitoring*, vol. 18, no. 5, pp. 554–573. [Online]. Available: <https://onlinelibrary.wiley.com/doi/abs/10.1002/stc.395>
- [48] U. Lagerblad, H. Wentzel, and A. Kulachenko, "Fatigue damage prediction based on strain field estimates using a smoothed kalman filter and sparse measurements," 2018, Conference paper, p. 2805 – 2817, cited by: 3. [Online]. Available: <https://www.scopus.com/inward/record.uri?eid=2-s2.0-85060378508&partnerID=40&md5=d07f0cf2900eece23813dd24e414b08a>
- [49] P. Ren and Z. Zhou, "Strain estimation of truss structures based on augmented kalman filtering and modal expansion," *Advances in Mechanical Engineering*, vol. 9, no. 11, 2017.
- [50] J. Zou, E.-M. Lourens, and A. Cicirello, "Virtual sensing of subsoil strain response in monopile-based offshore wind turbines via gaussian process latent force models," 2022. [Online]. Available: <https://arxiv.org/abs/2207.05901>
- [51] R. P. Palanisamy, S. Cho, H. Kim, and S.-H. Sim, "Experimental validation of kalman filter-based strain estimation in structures subjected to non-zero mean input," *Smart Structures and Systems*, vol. 15, no. 2, pp. 489–503, 2015.
- [52] M. Tarpø, T. Friis, B. Nabuco, S. Amador, E. Katsanos, and R. Brincker, "Operational modal analysis based stress estimation in friction systems," in *Nonlinear Dynamics, Volume 1*, G. Kerschen, Ed. Cham: Springer International Publishing, 2019, pp. 143–153.

- [53] A. Iliopoulos, W. Weijtjens, D. Van Hemelrijck, and C. Devriendt, "Fatigue assessment of offshore wind turbines on monopile foundations using multi-band modal expansion," *Wind Energy*, vol. 20, no. 8, pp. 1463–1479, 2017. [Online]. Available: <https://onlinelibrary.wiley.com/doi/abs/10.1002/we.2104>
- [54] A. Iliopoulos, W. Weijtjens, D. Van Hemelrijck, and C. Devriendt, "Full-field strain prediction applied to an offshore wind turbine," in *Model Validation and Uncertainty Quantification, Volume 3*, S. Atamturktur, T. Schoenherr, B. Moaveni, and C. Papadimitriou, Eds. Cham: Springer International Publishing, 2016, pp. 349–357.
- [55] A. Iliopoulos, R. Shirzadeh, W. Weijtjens, P. Guillaume, D. V. Hemelrijck, and C. Devriendt, "A modal decomposition and expansion approach for prediction of dynamic responses on a monopile offshore wind turbine using a limited number of vibration sensors," *Mechanical Systems and Signal Processing*, vol. 68-69, pp. 84–104, 2016. [Online]. Available: <https://www.sciencedirect.com/science/article/pii/S0888327015003350>
- [56] M. Mršnik, J. Slavič, and M. Boltežar, "Vibration fatigue using modal decomposition," *Mechanical Systems and Signal Processing*, vol. 98, pp. 548–556, 2018.
- [57] P. Bogert, E. Haugse, and R. Gehrki, "Structural shape identification from experimental strains using a modal transformation technique," in *44th AIAA/ASME/ASCE/AHS/ASC Structures, Structural Dynamics, and Materials Conference*, 2003, p. 1626.
- [58] H. P. Hjelm, R. Brincker, J. Graugaard-Jensen, and K. Munch, "Determination of stress histories in structures by natural input modal analysis," in *Proceedings of 23rd Conference and Exposition on Structural Dynamics (IMACXXIII)*, 2005.
- [59] M. Henkel, J. Häfele, W. Weijtjens, C. Devriendt, C. Gebhardt, and R. Rolfes, "Strain estimation for offshore wind turbines with jacket substructures using dual-band modal expansion," *Marine Structures*, vol. 71, p. 102731, 2020. [Online]. Available: <https://www.sciencedirect.com/science/article/pii/S0951833920300253>
- [60] M. Tarpø, B. Nabuco, A. Skafte, J. Kristoffersen, J. Vestermark, S. Amador, and R. Brincker, "Operational modal analysis based prediction of actual stress in an offshore structural model," *Procedia Engineering*, vol. 199, pp. 2262–2267, 2017, x International Conference on Structural Dynamics, EUROLYN 2017. [Online]. Available: <https://www.sciencedirect.com/science/article/pii/S1877705817336858>
- [61] A. Skafte, J. Kristoffersen, J. Vestermark, U. T. Tygesen, and R. Brincker, "Experimental study of strain prediction on wave induced structures using modal decomposition and quasi static ritz vectors," *Engineering Structures*, vol. 136, pp. 261–276, 2017. [Online]. Available: <https://www.sciencedirect.com/science/article/pii/S0141029617300378>
- [62] B. Nabuco, M. Tarpø, A. Aïssani, and R. Brincker, "Reliability analysis of offshore structures using oma based fatigue stresses," ser. International Conference on Offshore Mechanics and Arctic Engineering, vol. Volume 3A: Structures, Safety and Reliability, 06 2017, v03AT02A035. [Online]. Available: <https://doi.org/10.1115/OMAE2017-61730>
- [63] M. Henkel, W. Weijtjens, and C. Devriendt, "Fatigue stress estimation for submerged and sub-soil welds of offshore wind turbines on monopiles using modal expansion," *Energies*, vol. 14, no. 22, 2021. [Online]. Available: <https://www.mdpi.com/1996-1073/14/22/7576>
- [64] A. K. Chopra, *Dynamics of structures*. Pearson Education India, 2007.
- [65] S.-W. Seo, K.-J. Kim, and B.-K. Bae, "Estimation of operational strains from vibration measurements: an application to lead wires of chips on printed circuit board," *Journal of sound and vibration*, vol. 210, no. 5, pp. 567–579, 1998.
- [66] W. Heylen, S. Lammens, P. Sas *et al.*, *Modal analysis theory and testing*. Katholieke Universiteit Leuven Leuven, Belgium, 1997, vol. 200, no. 7.
- [67] N. M. M. Maia and J. M. M. e Silva, *Theoretical and experimental modal analysis*. Research Studies Press, 1997.
- [68] D. Ewins, "Modal testing: theory, practice and application, vol. 2," *Mechanical engineering research studies. Research Studies Press*, 2000.
- [69] E. H. Moore, "On the reciprocal of the general algebraic matrix," *Bull. Am. Math. Soc.*, vol. 26, pp. 394–395, 1920.

- [70] R. Penrose, "A generalized inverse for matrices," in *Mathematical proceedings of the Cambridge philosophical society*, vol. 51, no. 3. Cambridge University Press, 1955, pp. 406–413.
- [71] H. P. Hjelm, R. Brincker, J. Graugaard-Jensen, and K. Munch, "Determination of stress histories in structures by natural input modal analysis," in *Proceedings of 23rd Conference and Exposition on Structural Dynamics (IMACXXIII)*, 2005.
- [72] D. Li, H. Zhuge, and B. Wang, "The principle and techniques of experimental strain modal analysis," in *International Modal Analysis Conference, 7th, Las Vegas, NV*, 1989, pp. 1285–1289.
- [73] U. T. Tygesen, K. Worden, T. Rogers, G. Manson, and E. J. Cross, "State-of-the-art and future directions for predictive modelling of offshore structure dynamics using machine learning," in *Dynamics of Civil Structures, Volume 2*, S. Pakzad, Ed. Cham: Springer International Publishing, 2019, pp. 223–233.
- [74] F. P. Beer, E. R. Johnston, J. T. DeWolf, D. F. Mazurek, and S. Sanghi, *Mechanics of materials*. mcgraw-Hill New York, 1992, vol. 1.
- [75] Q. Liu, X. Qiao, Z. Jia, H. Fu, H. Gao, and D. Yu, "Large frequency range and high sensitivity fiber bragg grating accelerometer based on double diaphragms," *IEEE Sensors Journal*, vol. 14, no. 5, pp. 1499–1504, 2014.
- [76] Q. P. Liu, X. G. Qiao, J. L. Zhao, Z. A. Jia, H. Gao, and M. Shao, "Novel fiber bragg grating accelerometer based on diaphragm," *IEEE Sensors Journal*, vol. 12, no. 10, pp. 3000–3004, 2012.
- [77] A. N. Robertson, J. M. Jonkman, A. J. Goupee, A. J. Coulling, I. Prowell, J. Browning, M. D. Masciola, and P. Molta, "Summary of conclusions and recommendations drawn from the deepwind scaled floating offshore wind system test campaign," in *International Conference on Offshore Mechanics and Arctic Engineering*, vol. 55423. American Society of Mechanical Engineers, 2013, p. V008T09A053.
- [78] Bluewater, "Puffin - Documentation," Tech. Rep., 2022.
- [79] MARIN, "MARIN CABLE JIP WP21 - Offshore Basin Model Tests with Bluewater Floating Wind Solution," Tech. Rep., 2018.
- [80] Bluewater, "Calculations - Orcaflex Model Calibration using Model Tests," Tech. Rep., 2018.
- [81] Orcina, "Orcaflex - documentation." [Online]. Available: <https://www.orcina.com/webhelp/OrcaFlex/Default.htm>
- [82] HZ-Wind, "Standard wind turbine intake form," Tech. Rep.
- [83] J. Morison, J. W. Johnson, and S. A. Schaaf, "The force exerted by surface waves on piles," *Journal of Petroleum Technology*, vol. 2, no. 05, pp. 149–154, 1950.
- [84] "DNV-RP-C203 Fatigue design of offshore steel structures," DET NORSKE VERITAS AS, Standard, 2021.
- [85] P. Bogert, E. Haugse, and R. Gehrki, "Structural shape identification from experimental strains using a modal transformation technique," in *44th AIAA/ASME/ASCE/AHS/ASC Structures, Structural Dynamics, and Materials Conference*, 2003, p. 1626.
- [86] J. Dally and R. Sanford, "Strain-gage methods for measuring the opening-mode stress-intensity factor, k_I ," *Experimental Mechanics*, vol. 27, pp. 381–388, 1987.
- [87] Bluewater, "Report – TLP - Primary Structure - Design Report (FLS)," Tech. Rep., 2022.

A

Critical Locations BES TLP Model

The analysis is explained in the Primary Structure Design Report (FLS) with BES Document Number MMB-S-100-RP-4560-001-C [87]. It was performed using a dynamic and a structural model. From the global dynamic analysis, loads considered for the structural analysis were obtained as load time traces using 100 seastates. These loads are tendond loads, pontoon hydrostatic and dynamic pressures, column hydrostatic and dynamic pressures, accelerations (transverse and angular) and tower base loads (consisting of tower and turbine loads). A service life of 34 years is considered, a Designed Fatigue Factor (DFF) of 3 is assigned to the entire structure (it is a conservative generalisation), no additional Stress Concentration Fators (SCFs) are applied and the FLS FE model is made of shell elements. Then, the fatigue prone locations assessed in the analysis are indicated in [Figure A.1](#), they are checked using "E" and "F" SN-curves from DNV-RP-C203 [84].

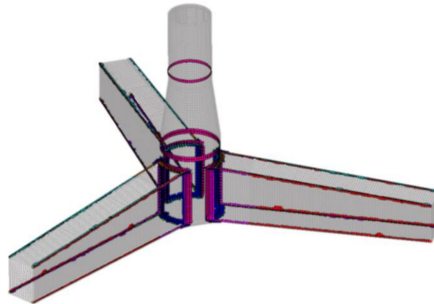


Figure A.1: TLP fatigue locations. [87]

The centroid principle stress time trace for every element are rainflow counted. The fatigue damage for all cycles is computed based on the fatigue SN curve approach with the assumption of linear cumulative damage (Palmgren-Miner rule) in accordance with DNV-RP-C203 [84] using [Equation A.1](#).

$$D = \sum_{i=1}^k \frac{n_i}{N_i} = \frac{1}{a} \sum_{i=1}^k n_i \cdot (\Delta\sigma)^m \quad (\text{A.1})$$

where: D = accumulated fatigue damage

\bar{a} = intercept of the design S-N curve with the log N axis

m = negative inverse slope of the S-N curve

k = number of stress blocks

$\Delta\sigma_i$ = stress range block

n_i = number of stress cycles in stress block i

N_i = number of cycles to failure at constant stress range $\Delta\sigma_i$

Then, damage per sea state simulation is scaled with the probability of occurrence and the total accumulated damage is then multiplied by the time factor (years of service life divided by the simulated time and the DFF). This gives as result the total fatigue utilisation of the fatigue location. Figure A.2 illustrates the locations of the TLP with maximum damage utilisation.

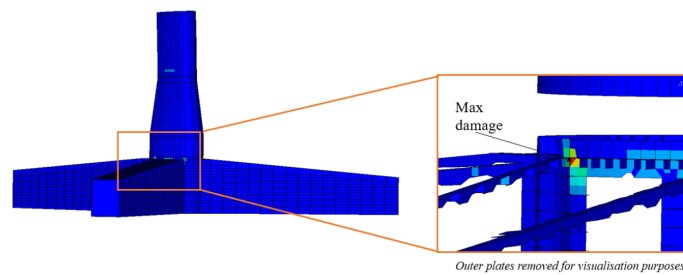


Figure A.2: Locations with maximum damage utilisation. [87]

B

Application of MDE to Simple Structure

B.1. Analytical Model

B.1.1. Introduction and Objective

To validate this methodology, the application of MDE in a simple structure is investigated. To start, an analytical model of a cantilever beam is used due to its simplicity. The analytical approach facilitates a better understanding of the process.

B.1.2. Model

The model is a 1D beam clamped on one side and free on the other one. The loading condition is a vertical point load (P) in the free end. It is divided into 10 elements. It has a length of 10 m and a rectangular cross-section with a height of 0.2 m and a width of 0.1 m. [Figure B.1](#) illustrates the model with the measured and the predicted DOFs.

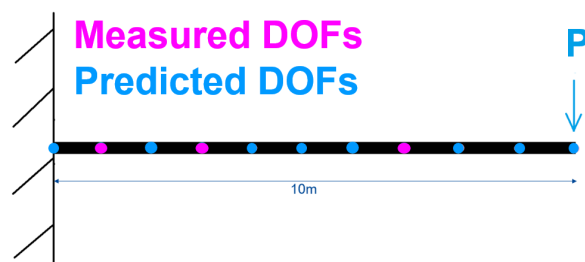


Figure B.1: Analytical model of cantilever beam.

B.1.3. Results

B.1.3.1. Modal Matrix

The mode shapes (ϕ) are obtained with the eigenvalue problem coming from the EOM. Recalling Equation 2.8, this is:

$$\omega_i^2 \mathbf{M} \phi_i = \mathbf{K} \phi_i \quad (\text{B.1})$$

For an Euler beam finite element (Figure B.2) with the DOFs being $\{\eta\}$, the element stiffness and mass matrices (i.e. \mathbf{K}_e and \mathbf{M}_e , respectively) are:

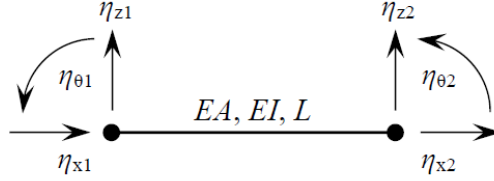


Figure B.2: Euler beam finite element.

$$\mathbf{K}_e = \begin{bmatrix} \frac{EA}{L} & 0 & 0 & -\frac{EA}{L} & 0 & 0 \\ 0 & \frac{12EI}{(1+\delta_s)L^3} & \frac{6EI}{(1+\delta_s)L^2} & 0 & -\frac{12EI}{(1+\delta_s)L^3} & \frac{6EI}{(1+\delta_s)L^2} \\ 0 & \frac{6EI}{(1+\delta_s)L^2} & \frac{(4+\delta_s)EI}{(1+\delta_s)L} & 0 & -\frac{6EI}{(1+\delta_s)L^2} & \frac{(2-\delta_s)EI}{(1+\delta_s)L} \\ -\frac{EA}{L} & 0 & 0 & \frac{EA}{L} & 0 & 0 \\ 0 & -\frac{12EI}{(1+\delta_s)L^3} & -\frac{6EI}{(1+\delta_s)L^2} & 0 & \frac{12EI}{(1+\delta_s)L^3} & \frac{6EI}{(1+\delta_s)L^2} \\ 0 & \frac{6EI}{(1+\delta_s)L^2} & \frac{(2-\delta_s)EI}{(1+\delta_s)L} & 0 & -\frac{6EI}{(1+\delta_s)L^2} & \frac{(4+\delta_s)EI}{(1+\delta_s)L} \end{bmatrix} \quad (\text{B.2})$$

$$\{\eta\} = \{\eta_{x1} \ \eta_{z1} \ \eta_{\theta1} \ \eta_{x2} \ \eta_{z2} \ \eta_{\theta2}\}$$

$$\delta_s = \frac{12EI}{A_s GL^2}$$

$$m_e = AL_s \rho_s$$

$$J_e = e^2 m_e / 2$$

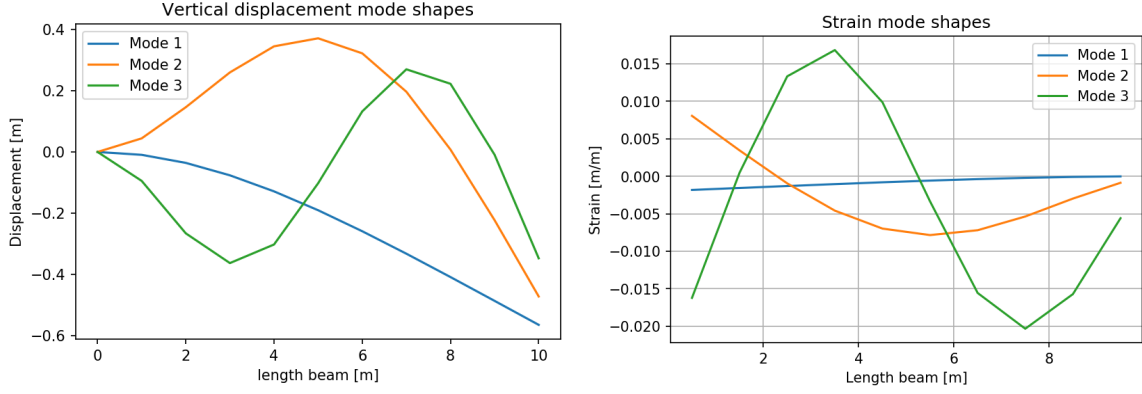
$$\mathbf{M}_e = \begin{bmatrix} m_e/2 & 0 & e & 0 & 0 & 0 \\ 0 & m_e/2 & 0 & 0 & 0 & 0 \\ 0 & 0 & J_e & 0 & 0 & 0 \\ 0 & 0 & 0 & m_e/2 & 0 & e \\ 0 & 0 & 0 & 0 & m_e/2 & 0 \\ 0 & 0 & 0 & 0 & 0 & J_e \end{bmatrix} \quad (\text{B.3})$$

These element matrices are assembled together to generate the stiffness and mass matrices of the entire structure.

The displacement modal matrix is composed by the mode shapes in terms of vertical displacement (η_z). The strain modal matrix is composed by the mode shapes in terms of strain ε , which is calculated as follows for each element:

$$\varepsilon_i = y_{max} \frac{\partial \theta}{\partial x} = y_{max} \frac{\eta_{\theta 2} - \eta_{\theta 1}}{L_{element}} \quad (B.4)$$

The first three modes are selected. The displacement and strain selected mode shapes are illustrated in [Figure B.3](#):



(a) Vertical displacement mode shapes.

(b) Strain mode shapes.

Figure B.3: Selected mode shapes.

B.1.3.2. Analytical Response

The vertical displacement is computed using the following equation:

$$\delta = \frac{P \cdot x^2}{6 \cdot EI} (3 \cdot L - x) \quad (B.5)$$

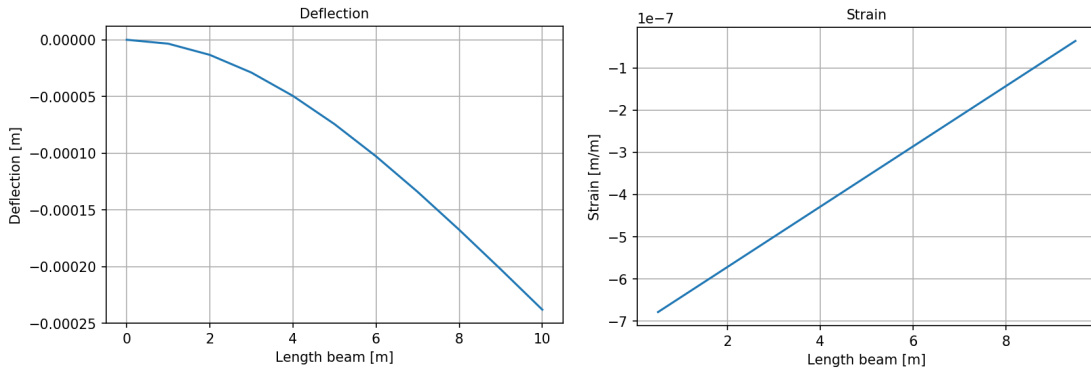
The strain is obtained as follows:

$$\varepsilon = -\kappa y_{max} = \frac{M}{EI} y_{max} \quad (B.6)$$

Where the bending moment is:

$$M = P \cdot (L - x) \quad (B.7)$$

The responses in term of deflection (i.e. vertical displacement) and strain are shown in [Figure B.4](#):



(a) Deflection response.

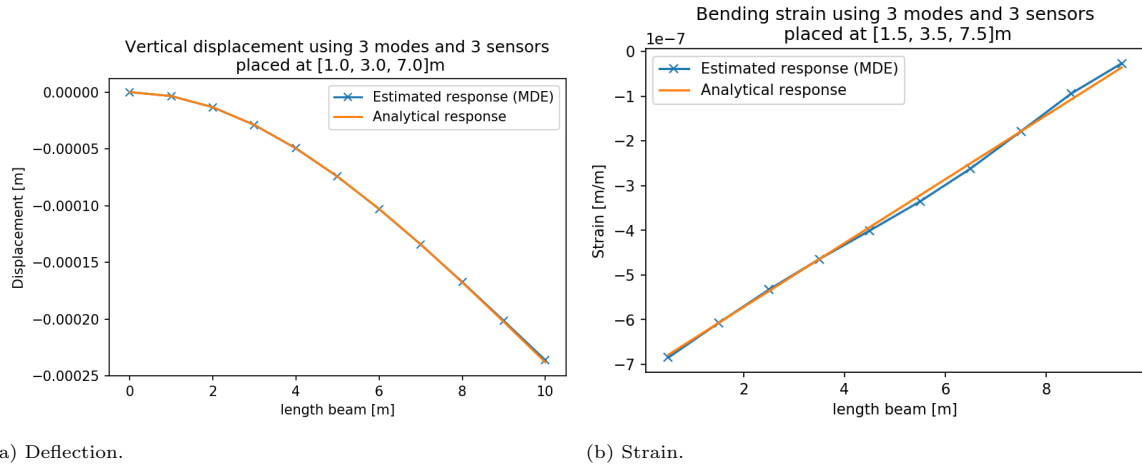
(b) Strain response.

Figure B.4: Analytical response.

B.1.3.3. Full-Field Response Estimation

Following the MDE methodology explained in [chapter 2](#), the displacement and the strain responses of the structure under the described loading conditions are predicted using 3 measured DOFs (i.e. sensors).

[Figure B.5](#) show the full-field displacement and strain estimations.



(a) Deflection.

(b) Strain.

Figure B.5: Full-field response estimations.

The accuracies of the estimations are 99.87% and 99.04% for the displacement and the strain responses, respectively. These accuracies are computed by obtaining the mean relative error of the entire beam and subtract it to the 100% of accuracy.

B.1.3.4. Conclusions

This analysis verifies the good performance of this methodology. It provides an accurate estimation of the full-field response estimation.

B.2. FE Model

B.2.1. Introduction and Objective

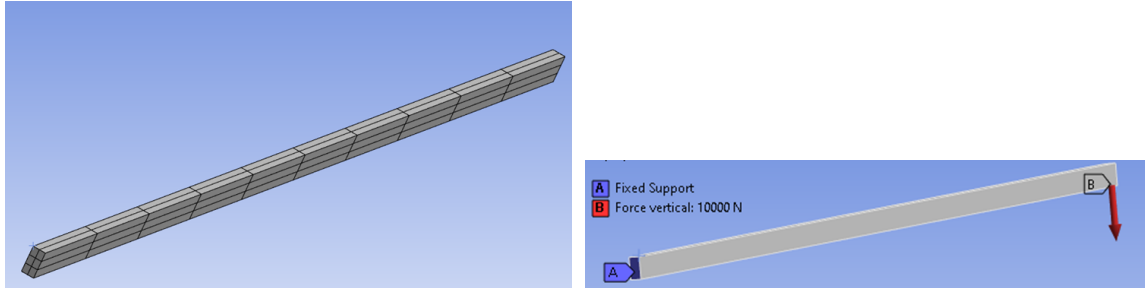
A FE model offers a representation that is closer to real-world structural complexities. Therefore, the application of MDE to a simple structure is expanded to a more complex and detailed model.

B.2.2. Model

The FE model pretends to represent the same beam as the previous (i.e. analytical) model. This model is modelled using Ansys Workbench. It has 1 m of length, and a rectangular cross-section with a height of 0.2 m and a width of 0.1 m. The analysis utilizes shell elements, as they efficiently capture the structural behavior without delving into the detailed response through the thickness, which is not a primary concern for the intended study. The length of the elements is the same as the previous model (i.e. 1 m), and they have a width of minimum of 0.05 m. This size enables having 2 elements per width

of the beam and 3 per height.

The boundary and loading conditions are the same as the previous model as well. The beam is clamped in one side and has a vertical point load at the free end. Figure B.6 illustrates the model with the mesh and the boundary and loading conditions.



(a) Mesh.

(b) Boundary and loading conditions.

Figure B.6: FE beam model.

B.2.3. Results

B.2.3.1. Modal Matrix

The complete modal matrix of the structure is obtained performing the modal analysis of Ansys Workbench. The strains in the longitudinal (i.e. X direction) for each mode are extracted. The modal selection is carried out by observation. The mode shapes are chosen if visually, they correspond to the structural response of the structure. For the vertical bending load applied, the modes with vertical bending are chosen. Figure B.7 shows the 3 selected mode shapes with the measured locations (they are the same as the previous model).

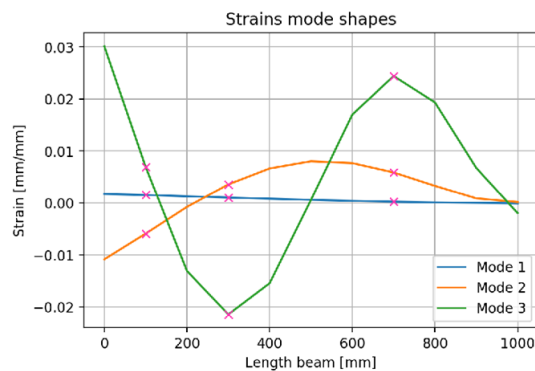


Figure B.7: Selected mode shapes.

B.2.3.2. Numerical Response

The static numerical response (simulating one sampling of the strain gauge) is obtained by performing the static structural analysis using Ansys Workbench with the boundary and loading conditions described previously.

B.2.3.3. Full-Field Response Estimation

By extracting the strain from the 3 measurement points and using the modal matrix with the 3 selected mode shapes, the modal expansion is performed. Figure B.8 illustrates the response estimation.

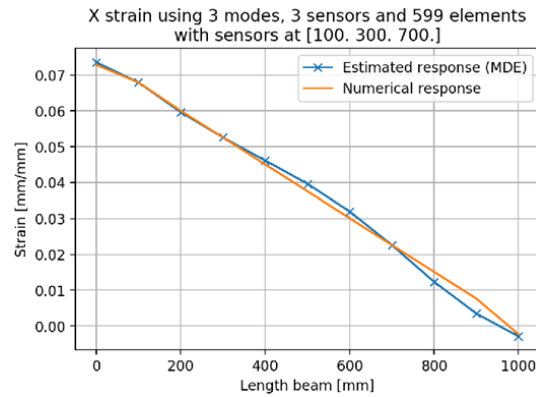


Figure B.8: Full-Field strain estimation.

The relative strain error in the hot spot (which in this case is the clamped side of the beam) is 0.98%, and the maximum relative error along the beam is of 5.7%.

B.2.4. Sensitivity Analysis

To see how sensitive this methodology is for the beam in front of various aspects, a sensitivity analysis is conducted.

B.2.5. Number of Sensors

An study is performed to obtain the optimal number of sensors in this structure. Figure B.9 shows the mean prediction error using different number of sensors. A convergence can be observed from 3 sensors, which indicates that it is the optimal amount of sensors to use.

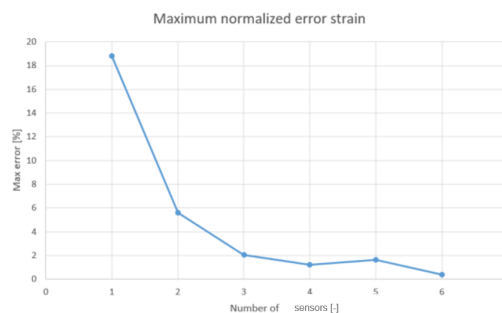
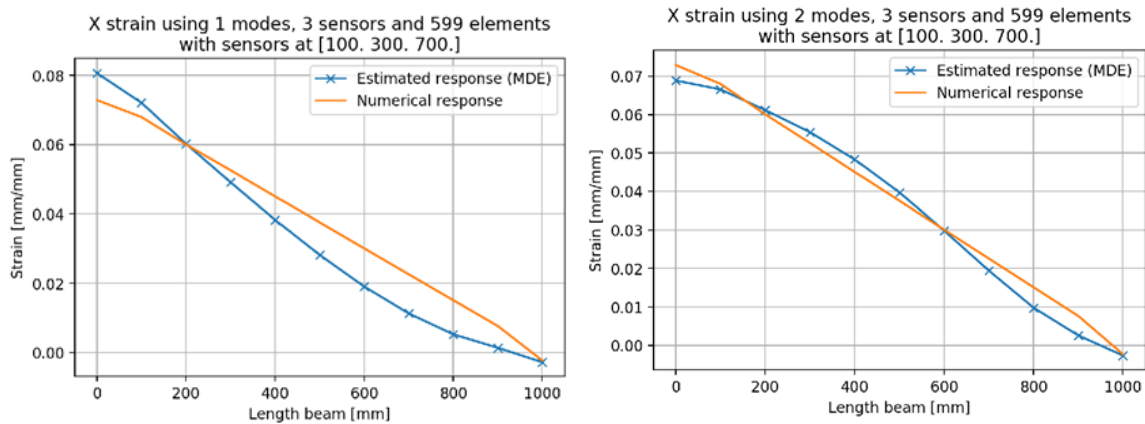


Figure B.9: Sensitivity analysis on number of sensors.

B.2.5.1. Number of Modes

The number of measurements has to be equal or higher than the number of considered modes [53]. However, it can be valuable to see how it affects to the predictions if the number of measurements

exceeds the number of modes. For this, the previous analysis has been performed using 1 and 2 modes with 3 sensors (i.e. higher number of measurements than modes). Figure B.10 shows the full-field strain estimations. If a comparison is made with the response estimation using the same amount of sensors than modes, it can be



(a) Response estimation using 1 mode and 3 sensors.

(b) Response estimation using 2 modes and 3 sensors.

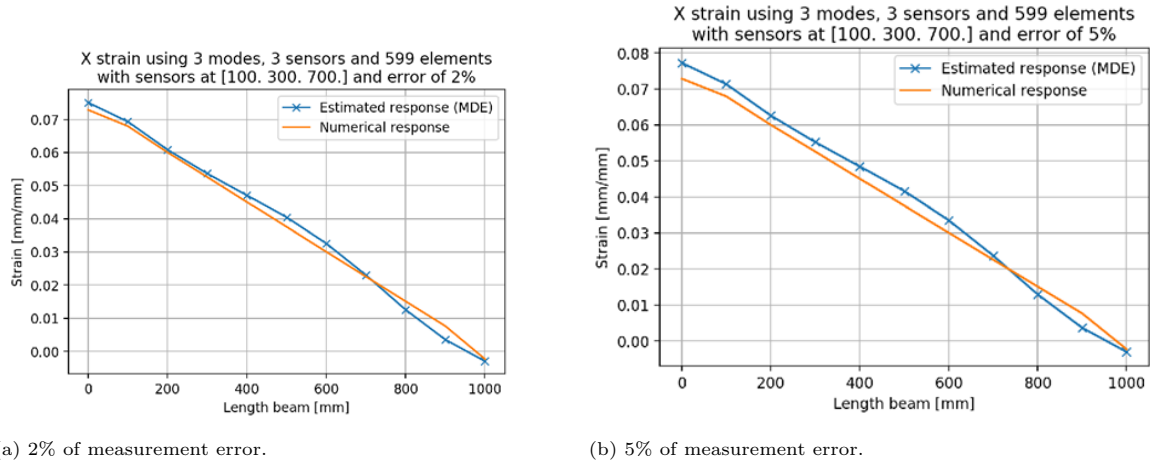
Figure B.10: Response estimations using less considered modes than number of sensors.

If a comparison is made with the response estimation using the same amount of sensors than modes, it can be observed that the response reconstruction is more accurate using 3 modes and 3 sensors than less amount of modes than sensors. The relative strain error in the hot spot using 1 mode is 10.7% and using 2 modes is 5.5%. Using 3 modes is 0.98%, which is notably smaller. The maximum relative strain error is also higher using 1 and 2 modes (15.5% and 7.3%, respectively) than using 3 modes (5.7%).

The justification of this is that if there are more sensors than modes, interpolation of the measurement is done and the measured data is not from the initially desired measurement locations.

B.2.5.2. Measurement Error

Strain gauges can have measurement errors, therefore, it can be valuable to see how this error affects the predictions. An error of 2% and 5% are induced in the measurements. Figure B.11 illustrate the response estimation with these induced errors in the measurement.



(a) 2% of measurement error.

(b) 5% of measurement error.

Figure B.11: Response estimations with measurement error.

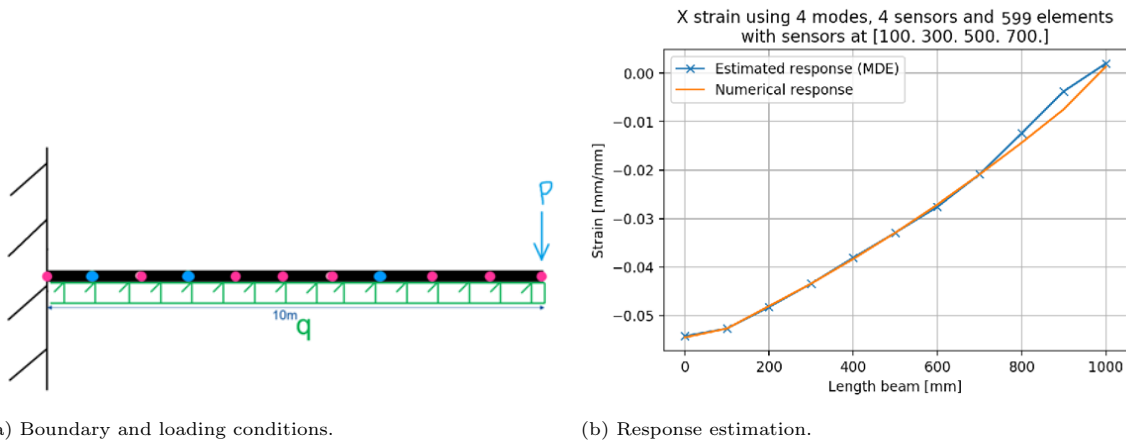
The maximum relative error in the predictions only increases a maximum of 0.5%, however, the relative error in the hot spot increases a 5%.

B.2.5.3. Varying Loading Conditions

To verify the versatility of the methodology, different loading conditions are tested.

Different vertical loading conditions

A more complex vertical loading conditions is applied to the structure. Figure B.12 shows the boundary and loading conditions (schematically) of this case and the response reconstruction.



(a) Boundary and loading conditions.

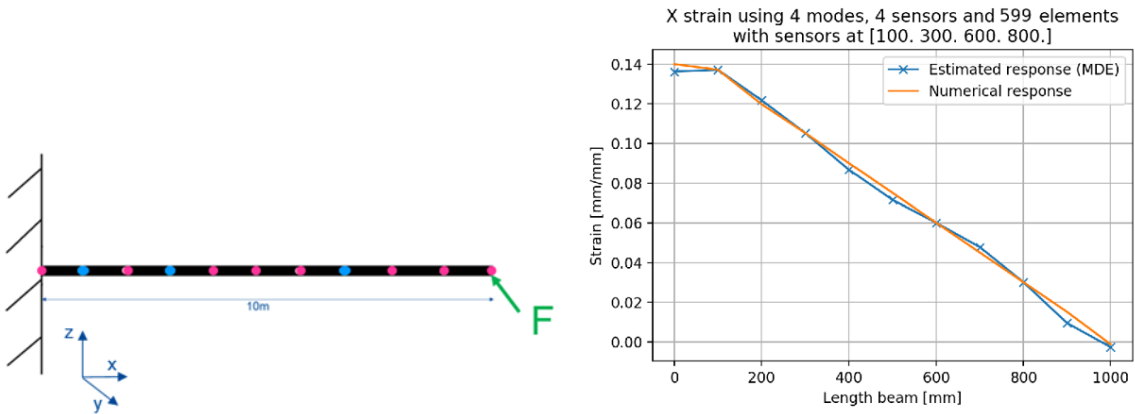
(b) Response estimation.

Figure B.12: Complex vertical loading.

The error of prediction only increases by 1%. It is acceptable.

Transverse loading

A transverse bending loading is applied. Figure B.13 illustrates the case study and the response estimation.



(a) Boundary and loading conditions.

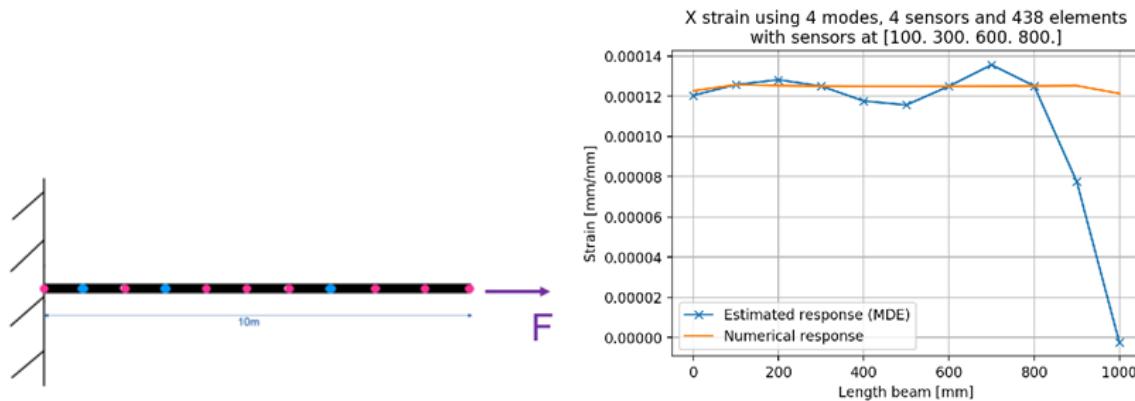
(b) Response estimation.

Figure B.13: Transverse loading.

The error of prediction is not higher than the error of estimating the vertical response.

Axial loading

An axial load is applied. Equation 3.13 shows this case study and the response prediction.



(a) Boundary and loading conditions.

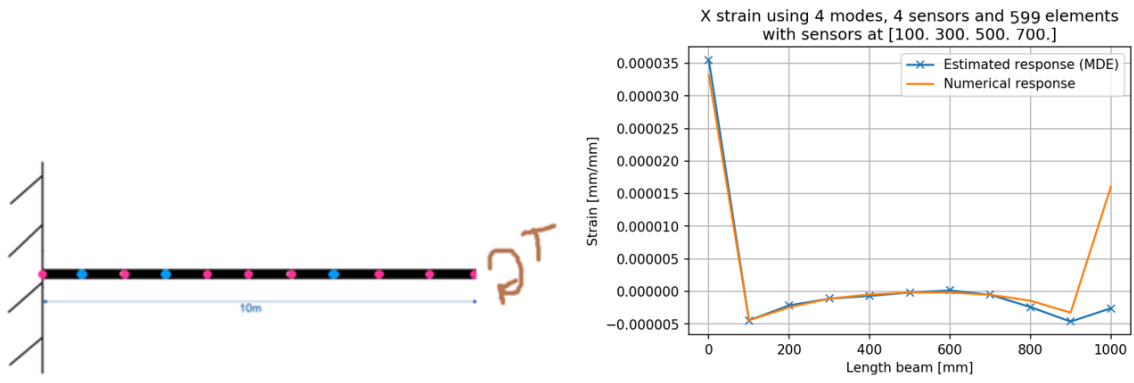
(b) Response estimation.

Figure B.14: Axial loading.

The error of prediction almost achieved the 100%, which is not acceptable by far.

Axial loading

Torsional loading is applied. Figure B.15 shows this case study and the response prediction.



(a) Boundary and loading conditions.

(b) Response estimation.

Figure B.15: Torsional loading.

The error of prediction increases to more than 50%, which is not a good estimation.

Combined bending loading

A loading combining vertical and transverse loading is applied. Using 2 sensor layouts (in each direction of the bending) with the same longitudinal sensor placement, the error of prediction is around 6%, which is acceptable.

B.2.6. Conclusions

Several conclusions can be extracted from this investigation. First of all, MDE can be applied a more detailed model using a simple structure. The response estimations are accurate. The number of sensors should be the same as the number of considered modes. Inducing measurement error increases particularly the strain estimation in the hot spot. For this structure, MDE is suitable for predicting responses due to bending loads (no matter in which direction). For axial and torsional loading, the response estimation are not accurate enough.

C

Response Analysis

load case		Max bending stress [Kpa]	Max axial stress (compression) [Kpa]	Max shear stress	Total stress [Kpa]
1	pontoon	3558	104	588	4250
	pontoon %	84%	2%	14%	
	column	3300	340	56	3696
	column %	89%	9%	2%	
2	pontoon	3659	105	593	4357
	pontoon %	84%	2%	14%	
	column	2854	344	46	3244
	%column	88%	11%	1%	
3	pontoon	4454	96	670	5220
	pontoon %	85%	2%	13%	
	column	820	338	20	1178
	column %	70%	29%	2%	
4	pontoon	4285	89	652	5026
	pontoon %	85%	2%	13%	
	column	1355	339	35	1729
	column %	78%	20%	2%	
5	pontoon	3648	89	586	4323
	pontoon %	84%	2%	14%	
	column	3243	339	77	3659
	column %	89%	9%	2%	
6	pontoon	5073	95	724	5892
	pontoon %	86%	2%	12%	
	column	1642	339	35	2016
	column %	81%	17%	2%	
7	pontoon	4960	148	753	5861
	pontoon %	85%	3%	13%	
	column	4946	334	125	5405
	column %	92%	6%	2%	

Figure C.1: Stress components contribution to total structural response.

Load case	H_s [m]	Wav_{dir} [°]	V_w [m/s]	$Windir$ [°]	V_c [m/s]	C_{dir} [°]
1	2	180	10	180	0	-
2	0	-	10	180	0	-
3	2	180	0	-	0	-
4	2	180	2	0	0	-
5	0	-	0	-	4	0
6	2	90	0	-	2	90
7	5	90	0	-	5	90

Table C.1: Characteristics of diverse load cases.